ABSTRACT

Fabrication and Demonstration of a Microfluidic Device Toward a Microfluidic-based
Microinjection for *Cx. pipiens* Embryo

Jeonghyeon Cheon, M.S.E.C.E.

Mentor: Seunghyun Kim, Ph.D.

According to the World Health Organization (WHO), more than 390 million people each year have reported being affected by mosquito borne diseases. In order to prevent epidemics of fatal diseases, altering mosquitoes through transfection, by inserting biological materials into vector embryos, deserves further development. The current transfection method is performed manually by a trained operator. However, the process is expensive and time-consuming, with a large variation in success rates dependent on operator skill. This research focuses on minimizing these limitations through the design and fabrication of a microfluidic system for *Cx. pipiens* mosquito embryo microinjection. In order to construct a microfluidic system with simple and low-cost fabrication processes, a 3D printer is employed. Fabrication processes were successfully developed and the device operation was validated. The microfluidic device shows feasibility toward microinjection for *Cx. Pipiens* embryos.

Fabrication and Demonstration of a Microfluidic Device toward a
Microfluidic-based Microinjection for Cx. Pipiens Embryo

by

Jeonghyeon Cheon, B.S.

A Thesis

Approved by the Department of Electrical and Computer Engineering

_____
Kwang Lee, Ph.D., Chairperson

Submitted to the Graduate Faculty of
Baylor University in Partial Fulfillment of the
Requirements for the Degree
of

Master of Science in Electrical and Computer Engineering

Approved by the Thesis Committee

_____
Seunghyun Kim, Ph.D., Chairperson

_____
Linda Olafsen, Ph.D.

_____
Cheolho Sim, Ph.D.

Accepted by the Graduate School
August 2019

_____
J. Larry Lyon, Ph.D., Dean

TABLE OF CONTENTS

LIST OF FIGURES

LIST OF TABLES

ACKNOWLEDGMENTS

I would first like to thank my thesis advisor Dr. Kim. He has always guided and led me in the right direction, both in research and life, with great patience and careful instruction. With his guidance, I could successfully write this thesis and had so many opportunities for growth. It has been a true honor and blessing in my life. I would also like to thank Dr. Sim. Without his support and assistance, the research could not have been successfully accomplished. I would also like to acknowledge Dr. Olafsen. I am extremely grateful for her valuable comments on this thesis. I'm deeply indebted to Patricia for all her support and I am grateful to Jennifer, Jessanne, and Caitlyn for the help in editing this thesis.

Finally, I must express my deep gratitude to my parents and to my brother for providing me with unfailing support and continuous encouragement throughout my years of study. This accomplishment would not have been possible without them. Thank you.

CHAPTER ONE

Mosquito-borne diseases

Mosquito-borne diseases, such as Zika virus (ZIKV), Dengue fever, Chikungunya virus (CHIKV), Yellow fever, and West Nile Virus (WNV) have a disastrous impact on mortality and morbidity in humans. These fatal infectious diseases are primarily transmitted to people through mosquitoes. With the effects of increased human movement [1], global warming [2], and rapid urbanization [3], the annual incidences of mosquito-borne diseases have been growing rapidly. People, infected from the diseased outbreak areas, carry and spread these fatal infectious diseases to other people in new regions [1]. Moreover, global warming changes ecosystems and gives new chances for the survival and proliferation of mosquitoes (e.g. increasing breeding sites, which are formed by high rainfall) [2]. Furthermore, many plastic containers and automobile tires, produced and used with drastic urban growth, provide ideal conditions for mosquito breeding and allow for large mosquito populations in populous cities [3].

Mosquito-borne disease has become a major health concern worldwide. ZIKV infection in pregnant women can cause microcephaly for infants. With microcephaly, the brain of the fetus does not develop properly, so the brain of an infected newborn baby is a smaller than normal [4]. A notable ZIKV outbreak occurred on Yap Island in the Pacific Ocean in 2007 [5]. 5005 of the 6892 Yap residents were infected and 919 of the infected people experienced clinical illness (e.g. fever, rash, and muscle pain, etc.). As shown in Figure 1.1, the number of countries and territories associated with ZIKV has greatly

increased recently and reached 70 countries and territories by 2016 [6]. In 2013, French Polynesia recorded approximately 20,000 reported cases [7]. Between 2015 and 2016, a major ZIKV outbreak occurred in Latin America and the Caribbean [8]. The World Health Organization (WHO) announced a temporary "Public Health Emergency of International Concern" in the region [8]. In 2015, at least 14 Brazilian states reported 440,000-1,300,000 suspected cases [9], [10] while more than 4000 cases of suspected microcephaly were reported in Brazil in 2016 [11], [12]. Between 2015 and 2016, a total of 51,473 suspected ZIKV infections were reported in Colombia, with 2090 laboratory-confirmed cases [13]. In 2016, 48 countries and territories in the Americas were affected by an ZIKV outbreak with 171,553 confirmed cases reported [14].
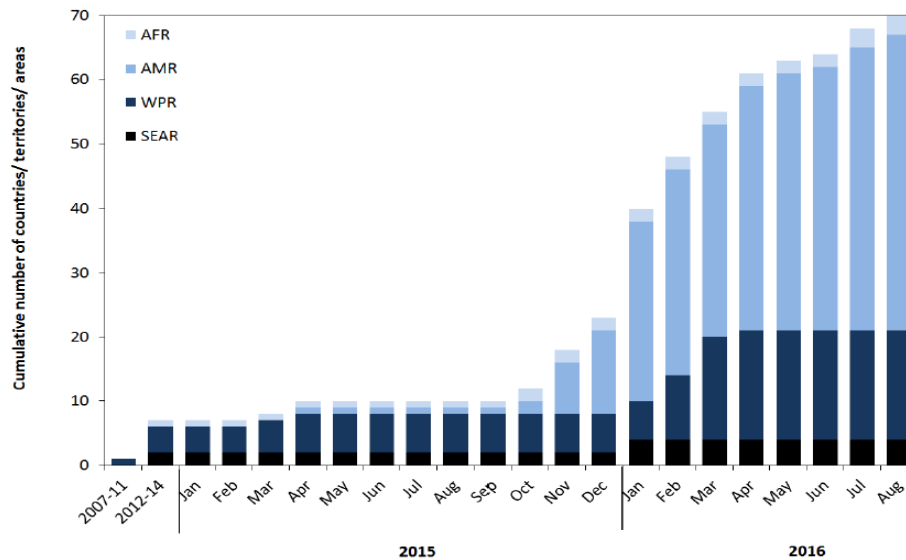
Figure 1. Cumulative number of countries and territories by WHO region reporting mosquito-borne Zika virus transmission in years (2007-2014), and monthly from 1 January 2015 to 24 August 2016 (Sub regions : Africa (AFR), Americas (AMR), Western Pacific (WPR), South-East Asia (SEAR)) [6].

2

Dengue fever is presently the most significant arboviral disease in humans. The symptoms of dengue virus infection are various, from mild fever to potentially deadly dengue shock syndrome [15]. Severe dengue, also called dengue Hemorrhagic Fever, is a potentially fatal complication. However, there are no effective antiviral agents for the treatment of dengue fever. Moreover, the recently developed dengue vaccine has fallen short of expectations in many trials [16]. Dengue fever is mainly found in the tropic areas, but there are local variations in risk depending on temperature, unplanned rapid urbanization, and rainfall [17]. In 2010, Bhatt *et al*. estimated approximately 390 million (range 284-528 million) Dengue infections, out of which 96 million (range 67-136 million) were clinically obvious. The global incidence of dengue shows rapid growth in this recent decade [18]. Figure 1.2 (a) shows the number of dengue cases indicating a drastic increase from 2.2 million in 2010 to 3.2 million in 2015 [15], [19]. The total number of deaths reported to WHO during 1990-2015 is shown in Figure 1.2 (b) [15]. In 2015, the Americas alone reported 2.35 million cases of dengue, with 10,200 severe dengue cases, which claimed 1,181 lives. In the same year, Delhi, India, recorded over 15,000 cases and the Island of Hawaii, United States of America, reported 181 cases [15]. In 2016, large dengue outbreaks emerged worldwide. More than 2.38 million cases were reported in the Americas in 2016, of which Brazil alone reported approximately 1.5 million cases, including 1,032 dengue deaths. The Western Pacific Region declared an outbreak with more than 375,000 dengue suspected cases in 2016, including 176,411 cases in the Philippines and 100,028 cases in Malaysia. More than 7,000 dengue suspected cases were also reported in the Solomon Islands in the same year. In the African Region, Burkina Faso was affected by a localized outbreak of dengue with 1,061 probable cases in 2016. In 2017, 584,263 cases of

dengue were reported in the Americas. According to the WHO, 500,000 people with severe dengue need hospitalization each year, and 12,500 people die because of severe dengue.

(a)

(b)
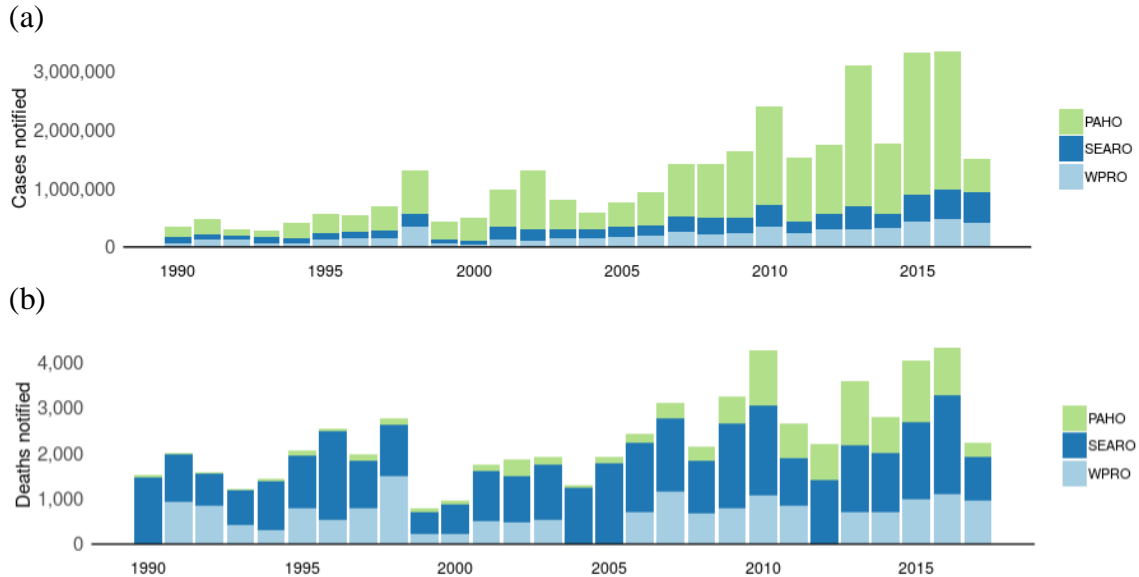
Figure 1.2. (a) The number of suspected or laboratory-confirmed dengue case notified to WHO since 1990 (b) the number of death notified to WHO Since 1990 [20]. (Regional offices: Pan American Health Organization (PAHO), South East Asia Regional Office (SEARO), Western Pacific Regional Office (WPRO)).

Yellow fever causes fever, headache, jaundice, muscle pain, nausea, vomiting and fatigue [20]. The fatality rates of yellow fever in reported cases are higher than 75%. While there is an effective vaccine to prevent yellow fever disease [21], large epidemics of yellow fever can still outbreak when infected people spread the virus into highly populated areas with high mosquito density [13], [20]. Many African and American countries are still in danger of yellow fever [13]. Outbreaks of Yellow fever in Africa in the 1960s and the late 1980s brought disaster, with more than 200,000 cases [22]. In 2013, 78,000 deaths related to outbreak in Africa were estimated, together with 130,000 cases of infections [23]. As shown in Figure 1.3, a total of 4,347 suspected, 884

4

confirmed, and 377 deaths were reported in Angola while 2,987 suspected, 77 confirmed, and 121 death were recorded in Congo in 2016 [24]. Between 2017 and 2018, Brazil recorded 723 confirmed case of yellow fever, including 237 deaths [25]

(a)

(b)
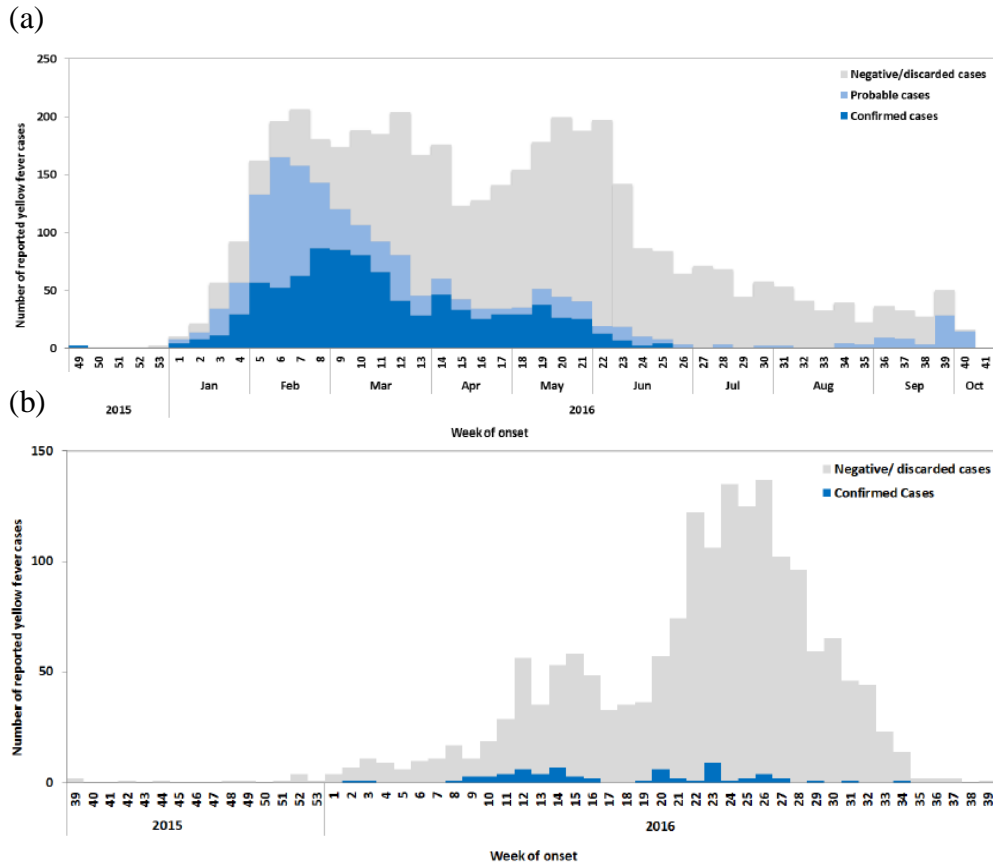
Figure 1.3. (a) National weekly number of confirmed, probable and negative yellow fever cases in Angola, 5 December 2015 to 13 October 2016 (b) National weekly number of confirmed and negative yellow fever cases in Democratic Republic of the Congo, 21 September 2015 to 26 October 2016 [28].

The symptoms of CHIKV include high fever, debilitating arthralgia, and headache. Relieving the symptoms is the only treatment for CHIKV because there is no vaccine for it [26, 27]. Outbreak of CHIKV has contributed to serious public health and economic damage [26], [28]. More than 1.9 million cases have been reported in India, Indonesia, Maldives, Myanmar and Thailand since 2005 [27]. Cases of CHIKV have

been reported in 45 countries and territories in North, Central, and South America and the Caribbean Islands [29]. In 2006, La Reunion Island had 47,000 cases [29]. Almost 40 % of the population in La Reunion Island experienced CHIKV disease. India also experienced a large Chikungunya outbreak during 2006-2007 [27]. Table 1.1 summarizes the number of reported CHIKV to the Pan American Health Organization (PAHO) during 2014-2017 [30]–[33]. A total of 2,176,771 suspected, 242,022 confirmed, and 428 death cases were reported during this period. The Americas recorded 693,489 suspected cases and 37,480 confirmed cases of Chikungunya in 2015, of which Colombia contributed 356,079 suspected cases. In 2016, 351,334 suspected and 152,769 laboratory confirmed cases reported to the PAHO regional office, of which Brazil had 265,000 suspected cases, and Bolivia and Colombia recorded 19,000 suspected cases. In the African region, Kenya was affected by a CHIKV outbreak with over 1,700 suspected cases reported in 2016 [27]. Africa, Southeast Asia, and Americas are now at risk of CHIKV epidemic [26]–[28], [30]–[33].

Table 1.1. The number of reported CHIKV cases notified to the PAHO since 2014.

Year	Suspected cases	Confirmed cases	Deaths
2014	1,071,696	22,796	169
2015	693,489	37,480	74
2016	351,334	152,769	172
2017	60,252	28,977	13
Total	2,176,771	242,022	428

West Nile Virus (WNV) can result in serious neurological disease and can ultimately be fatal [34]. WNV is most prominent in Africa, Europe, the Middle East, North America and West Asia. Human infection is most often transmitted through the bite of infected mosquitoes. When mosquitoes bite and suck the blood of infected birds,

the mosquitoes become infected. Around 80 % of infected people are asymptomatic (no symptoms) and about 20 % of people develop West Nile fever or severe West Nile disease (called neuroinvasive disease). Severe disease causes headache, neck stiffness, high fever, coma, muscle weakness, paralysis, etc. There are no vaccines for treating or preventing WNV in people. In 2000, Israel reported 417 confirmed cases with 326 hospitalizations, including 33 deaths [35]. Romania reported 393 confirmed cases in 1996 and 54 cases with neuroinvasive infection in 2010 [36]. In 2010, 81 cases of West Nile neuroinvasive disease occurred in the region of Central Macedonia, northern Greece [37]. Between 1999 and 2017, 48,183 confirmed WNV disease cases (Neuroinvasive disease: 22,999 cases, Non-neuroinvasive disease: 25,184) were reported in 47 states of the United States (US) and the District of Columbia, including 2,163 death [38]. The most recent update in 2017 reported 2,097 cases of WNV disease in humans in the US, including 146 deaths. Out of them, 1,425 cases were confirmed to be neuroinvasive disease, giving a national incidence of 0.44 per 100,000 population.

There are various types of mosquitoes such as *Aedese aegypti, Culex pipens, Anopheles gambiae*, etc. Out of those, *Aedese aegypti* and *Culex pipiens* are two mosquito species causing the majority of mosquito-borne diseases discussed above. *Aedes aegypti*, also known as yellow fever mosquito, is a vector that transmits ZIKV, Dengue fever, CHIKV and Yellow fever [39], [40]. A vector is an organism that transmits infections by transferring viral infection from one host to another, but does not produce the disease itself. As shown in Figure 1.4 (a), the mosquito has a white striped pattern on its legs and the upper surface of its thorax [41]. This mosquito species can be found in tropical and subtropical regions all over the world [42]. Only female mosquitoes bite and suck blood

[41]. Female mosquitoes find a host using chemical compounds (e.g. ammonia, carbon dioxide and lactic acid) emitted from mammals [41]. They spread viruses as carriers, by biting an infected person and transmitting the virus through biting other people [39].

During the day, they deposit dozens of eggs above the water line, which contain organic materials such as decaying leaves, algae, and etc., in natural locations (e.g. plant axils and tree holes) or artificial containers (e.g. flower pots, animal dishes, buckets, and etc.) [40]. Their larvae generally eat small aquatic organisms such as particles of plants and animal in the water for growing [40]. In 7-8 days the aquatic portion is complete and they become adult mosquitoes [40]. The adult mosquitoes can live around three weeks [40].

Culex pipiens is a mosquito that can spread West Nile Virus. As shown Figure 1.4 (b), an adult female mosquito has uniform brown colored legs and striping on the abdominal segments [43]. They are the most widely distributed mosquito in the world. They usually prefer to bite birds more than humans. However, if they have the opportunity, *Culex pipiens* will feed on people. These mosquitoes can use natural locations and artificial containers with still water (e.g. buckets, flower pots, or bird baths) to lay their eggs. These mosquitoes lay eggs in rafts of 50-150 or more, and they stick together and float above the water. The entire aquatic cycle (i.e., from egg to adult) can occur in 7-9 days. The life span of adult mosquitoes is normally a few weeks. However, they can sometimes survive for several months during the winter.
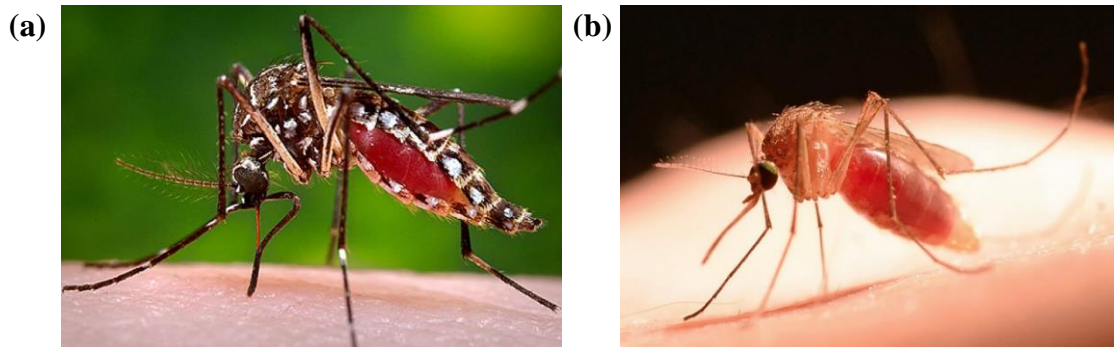
Figure 1.4 (a) Female *Aedes aegypti* mosquito (b) Female *Culex pipiens* mosquito.

The best way to suppress mosquito-borne diseases is by minimizing the population of the mosquitoes in the area, a process called a vector control. There are several different vector control approaches, which include insecticide-based control and biological control. The conventional mosquito population suppression method is insecticide-based control. This method used by mosquito-control organizations, or companies have sprayed insecticides (e.g. DDT (dichlorodiphenyltrichloroethane), Malathion, Permethrin, etc.) using truck or aircraft mounted sprayers. *Ae. aegypti* vector control was considered to be successful through systematic insecticide-based control method using DDT in the early 20th century [44] and 22 countries declared the absence of the species by the early 1960s [45]. However, *Ae. aegypti* had not been completely eradicated and reappeared. Furthermore, it turned out it is difficult to suppress the population over the long-term because the mosquitoes lay their eggs in areas of reduced exposure to insecticides (e.g. plastic containers) [46]. These "safety sites" are diverse and widely distributed, especially in areas of dense human populations. Also, the insecticide-based control method has some limitations such as slow operational response, ineffective timing of application, and high costs. Mosquitoes eventually develop insecticide resistance, which in turn reduces efficacy of the insecticide spraying method. Moreover, insecticide is toxic for non-target species

(e.g. bees, butterflies, lady bugs, etc.) which may cause serious environmental and health problems [46], [47].

As a consequence, the development of new and effective vector control methods is needed. Biological control (transfection-based vector control) is one of the most attractive alternatives. Biological control produces genetically modified mosquitoes by inserting biological materials into embryos, which is called transfection.

The transfection process uses genetically-modified male mosquitoes to ultimately suppress the overall mosquito population. Through transfection, genetically-modified male mosquitoes carry a lethal transgene, which produces a protein called tetracycline repressible transactivator protein (Ttav) to inhibit the activity of a cell [48]. The genetically-modified male mosquitoes are released to mate with wild female mosquitoes, and thereby suppress their offspring by passing the lethal transgene causing death before adulthood [49]. A trial performed in the Cayman Islands in 2010 shows that a release of genetically-modified male mosquitoes subdued the local *Ae. aegypti* population by 80%. In Brazil in 2015, another trial showed the reduction of *Ae. aegypti* population by 95% [50]. There is great potential in the application of biological control to reduce the risks of fatal mosquito-borne diseases. An in-depth overview of transfection methodology will be provided in the Chapter 2.

CHAPTER TWO

Transfection

In general, the process introducing genetic biomolecules, such as proteins, nucleic acids, and antibodies, into cells or embryos to make genetically manipulated cells or embryos is called transfection. There are two categories of transfection, which are stable transfection and transient transfection [51]. In stable transfection, the foreign DNA is combined with a genome in the target cell [52]. On the other hand, with transient transfection, the foreign DNA is not combined with the genome, so changes are only temporarily expressed [51]. Transfection is a significant tool for genetic engineering, *in-vitro* fertilization, and drug development. The increased need of a transfection method with a high transfection efficiency, minimal effect on normal physiology, and ease of use has led to the development of various techniques. There are three different methods used for transfection: biological, chemical, and physical transfection methods (Figure 2.1).

Biological transfection methods, which deliver DNA into the cell using a genetically modified virus [53], is the most widely applied method in clinical research. There are two types of biological transfection methods: *Ex vivo* viral and *in vivo* viral gene transfection [54]. *Ex vivo* transfection exposes the cultured cells to a viral vector in order for delivering the desired gene. Subsequently, the infected cells are reinserted into the organism after growing in the laboratory. *In vivo* viral transfection (e.g. gene therapy) directly inserts viral vectors containing the desired gene into the model organism through the blood stream for stable genomic integration. These biological transfection methods

are highly efficient and simple. However, disadvantages are high cytotoxicity, high-cost, and limited targeting of specific cell types. Moreover, a virus package has limited carrying capacity for a foreign gene [54], [55]. To address these issues, non-viral transfection methods such as chemical and physical methods have been developed.
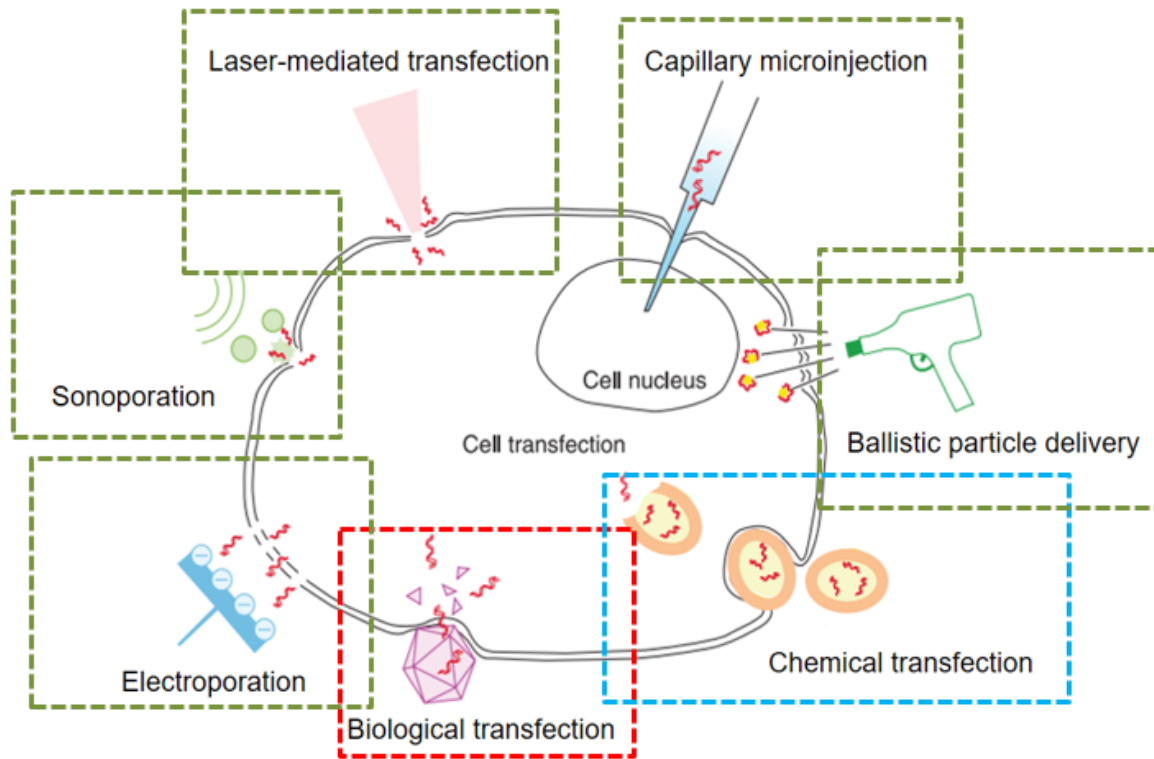
Figure 2.1. Different types of transfection methods: biological transfection method (red dot-square), Chemical transfection method (blue dot-square), Physical transfection method (green dot-square) [56].

Chemical transfection methods use conjugated reagents to carry genetic biomolecules into cells or embryos. These methods are commonly used in laboratory research [57]. Cationic polymer (e.g. DEAE-dextran or polyethylenimine (PEI)), calcium phosphate (one of the cheapest methods), cationic lip (the most popular method), and cationic amino acid are frequently used to coat nucleic acids to promote absorption of

nucleic acids by the cell membrane and transport them into the cells [58]–[60]. The advantages of chemical transfection methods include no mutagenesis, no size limitation on the packaged nucleic acid, no extra-carrying DNA and relatively low cytotoxicity [54], [55]. However, these processes show low transfection efficiency influenced by various factors (e.g. nucleic acid/chemical ratio, cell membrane conditions, solution pH, etc.) [54], [55].

Physical transfection methods directly deliver biomolecules into cells and embryos. Various physical methods have been developed to physically open holes on the cell membrane and deliver biomolecules into it. This is the most widely used method for mosquito transfection, for reasons addressed later in this chapter. The details of various physical transfection methods are presented here: ballistic particle delivery, electroporation, sonoporation, laser-mediated transfection, and capillary microinjection.

Ballistic particle delivery (also known as gene gun) transports the genes into the cells using microscopic gold particles [61], [62]. John *et al*. demonstrated a biolistic transfection of plasmids into cultured Human Embryonic Kidney (HEK) and organotypic brain slices through a hand-held gene gun (Figure 2.1) [61]. The injection process was performed in three steps. First, copies of the DNA were coated on the gold particles (diameter: ~ 1 μm), which are inert, non-toxic, and smaller than transfected cells. Second, the gold/DNA particles were moved into a cartridge. Finally, as shown in Figure 2.2 (b), the gold/DNA particles are shot at cells by air pressure. When the gold/DNA particles pass through the cell nucleus, the gene combined with DNA of the chromosome. While ballistic particle delivery has merits, such as simplicity, versatility, high reproducibility,

cell type independence, and low DNA consumption, the method generally requires costly

instruments and causes physical damage to cells.
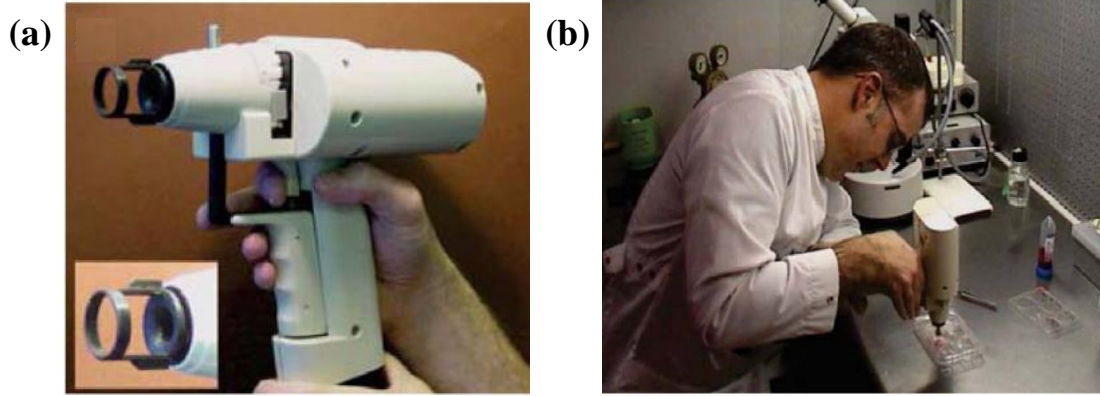
Figure 2.2. (a) Helios gene gun. (b) The gold/DNA particles are shot at cells [61].

Electroporation is another physical method using high-voltage electrical pulses to

make reversible holes in the cell membrane [63]–[67]. There are multiple applications for

this method. Ino *et al*. demonstrated selective transfection of myelinating Schwanne cells

(SCs) in the rodent sciatic nerve with electroporation [65]. In this *In vivo* electroporation

method, they showed highly efficient simultaneous expression of multi transgenes. Shi *et al.* reported a DNA transfection system for the crayfish hematopoietic tissue (Hpt) cells

using electroporation [66]. They could achieve high transfection efficiency, more than

30% with the relative cells' viability ~50%. Zhao *et al*. designed a flow-through cell

electroporation device (FED) by combining a needle electrode array in a large flow

tube as shown in Figure 2.3 [67]. The large flow tube allows high flow rate, low shear

force, and simple flow characterization while the evenly distributed needle electrode

array generates a uniform-distributed electric field with a low voltage. As shown in

Figure 2.3(c), the cells were mixed with nucleic acid and electroporation buffer

solution. Then, the cells were loaded into the FED. The loaded cells were electroporated by applied voltage in electroporation chamber and the nucleic acids were introduced into the loaded cells. The electroporated cells were unloaded into the outlet and gathered for culture. Their device showed 67% high nucleic acid transfection efficiency and 80% cell viability on cell lines. Furthermore, RNA was successfully released into freshly isolated cells and the erythrocyte was re-transfected back as RNA carrier. The flow-through electroporation device achieved a high cell processing speed (2.25×10^7 cells/minute). The electroporation method is simple and rapid so that a large number of cells can be transfected in short time in optimum electroporation conditions. Furthermore, it can be used with a wide range of cell types. Still, in spite of all these benefits, extended electrical pulse exposure can result in cellular death due to the membrane damage [64]. Moreover, the number of nucleic acids cannot be exactly controlled but rather randomly injected into the cell so it results in a non-quantitative reagent transfection.
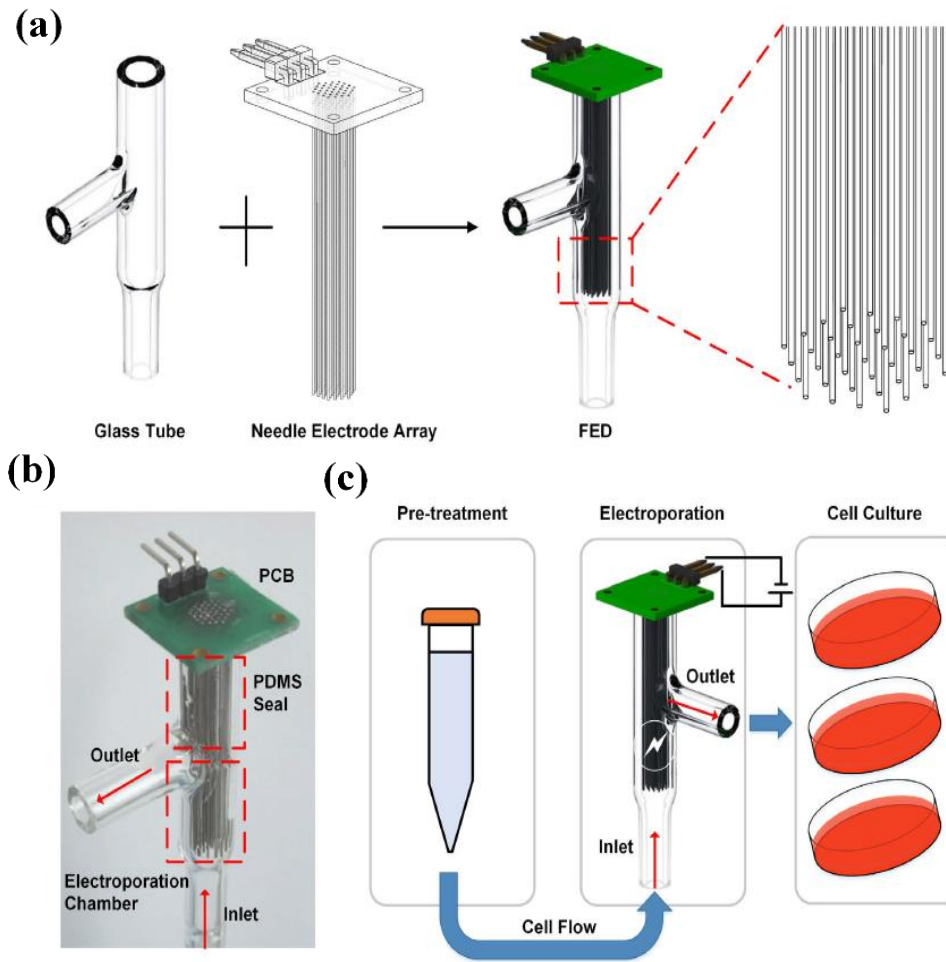
Figure 2.3. A flow- through cell electroporation device (FED) and its working process. (a) The schematic of the FED structure. (b) A photo of FED, the PDMS seal area and the electroporation chamber are marked with red dashed boxes. (c) The operation process of FED [67].

Sonoporation method uses ultrasound which changes the permeability of the cell membrane and produces transient hole through heating and cavitation [68], [69]. Le Gac *et al.* used a single laser-induced cavitation bubble for the sonoporation of HL60 (human promyelocytic leukemia) suspension cells in a microfluidic confinement as shown in Figure 2.4 [70]. The microchamber (in Figure 2.3 (b)) was exposed by a frequency-doubled pulsed laser (Nd:YAG laser at 532 nm, 6 ns pulse duration) to make cavitation

16

bubbles with 10–30 μs life times. Membrane poration of cells can be generated by the

cavitation bubbles. Cells, which are located closer than 0.75 R_{max} (maximum bubble

radius) from the cavitation bubble center, have holes with a probability of 0.75%.

However, if cells stayed away more than 4.0 R_{max} from the cavitation bubble center, then

they were not influenced. Abdalkader *et al.* demonstrated *in vivo* gene transfection in

mice left limb muscles using sonoporation [71]. They used stable nano-sized bubbles

through the mechanical agitation method with perfluorocarbon gases. Tsuchiya *et al.*

reported sonoporation-mediated gene delivery through polyethylene glycol (PEG)-grafted

polymeric carriers, which is specifically reacted with hyperactivated protein kinase A

(PKA) [72]. Sonoporation effectively delivered PEG-grafted polymeric carrier/DNA

polyplexes (the hydrophilic PEG layer) into the cells. These methods are simple, but cells

can disintegrate if overexposed. Moreover, similar to electroporation, because the number

of nucleic acids cannot be exactly controlled, but are rather randomly injected into the

cell, it causes non-quantitative reagent transfection.
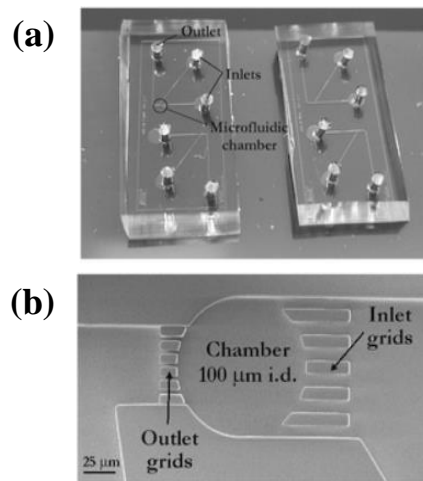
Figure 2.4. (a) Photograph of microsystems. (b) A scanning electron microscope (SEM) image of microchamber [70].

Laser-mediated transfection produces a transient hole using a pulsed laser [73], [74]. The advantages of laser-mediated transfection method are (1) it can be used for small cells and (2) it can produce holes at any location on the cell. Thobakgale *et al*. reported successful injection of green fluorescence protein plasmid (pGFP) and Sox-17 plasmid DNA (pSox-17) to change the behavior of mouse embryonic stem cells (mESCs) using laser-mediated transfection [75]. To make the holes on the cell membrane, they used femtosecond (fs) laser pulses (laser power: 6 μW, pulses: 128 fs, and pulse repetition rate: 1 kHz) under a home-built microscope system.

Overall, these physical transfection methods (ballistic particle delivery, electroporation, sonoporation, laser-mediated transfection) improve transfection efficiency, but, they show non-quantitative reagent transfection because the number of nucleic acids cannot be exactly controlled but are rather randomly injected into the cell.

Capillary microinjection, another physical transfection method, overcomes the limitations of other physical methods. Transfection is performed by direct insertion of a microneedle. The capillary microinjection has successfully been used to inject the known amount of various molecules such as lipids, proteins, and drugs into single cells. However, it is a highly labor-intensive and operator-dependent method, usually suffering from a low throughput and high variation of success rates among operators based on their skills (e.g. orienting the needle, holding pipettes in space and inserting the needle into cells). In order to improve the throughput and reduce the technical variation among operators, semi- and fully-automated micro-robotic injection systems have been developed [76], [77]. Chun *et al*. demonstrated suspended cell injection using a microelectromechanical systems (MEMS) device as shown in Figure 2.5 [78]. The

MEMS device consists of microchambers for holding cells and a microarray injection capillary (diameter: 5 μm, length: 30 μm, thickness: 1 μm). Cells were loaded in the microchambers and fixed with suction. Then, the microarray injection capillary was aligned along the pattern of the microchambers and inserted into the cells. Next, reagents were delivered into the cells through pneumatic pressure. This device shows high throughput microinjection but requires rather complicated and expensive fabrication processes.
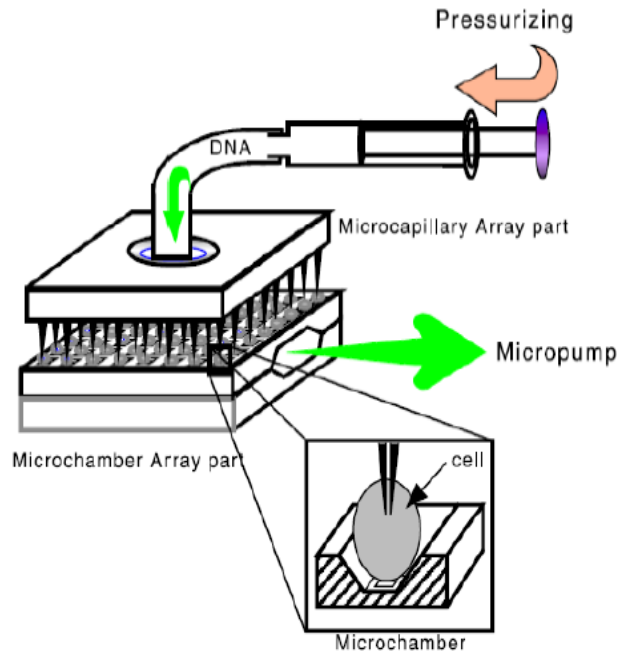
Figure 2.5. Microinjection MEMS device [78].

Fully-automated micro-robotic injection systems were developed by Gentil *et al*. and Wang *et al*. Gentil *et al*. demonstrated precise cellular injections using redesigned the atomic force microscope (AFM) [76]. As shown in Figure 2.6 (a), the AFM tip was inserted to any location inside the cell through the precise positioning and force feedback

control of the AFM under an inverted microscope. The tip was modified to have an internal empty core to introduce biomolecules into cells as seen in Figure 2.6 (a). They injected Lucifer yellow CH(LY) into the Hela cells with a 100% success rate.
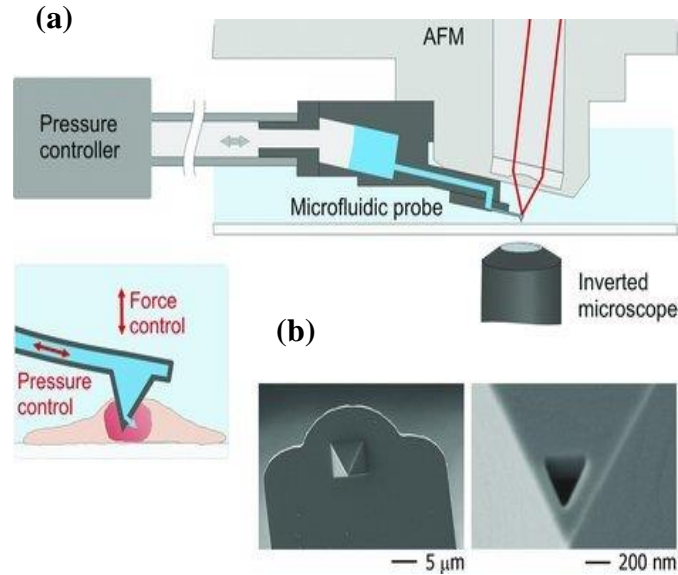
Figure 2.6. (a) Schematic of the intranuclear injection using fluidic force microscopy (b) Scanning electron micrographs of a FluidFM injection probe [76].

Wang *et al*. reported a fully automated zebrafish embryo injection using a microrobotic system in Figure 2.7 [77]. A vacuum-based embryo holding device is shown in Figure 2.7. Evenly aligned holes (400 mm diameter) are integrated with a vacuum source through a backside channel. Zebrafish embryos are trapped at each through-hole on the device by a sucking pressure (50-178 mmHg) and then injected under the microscope using a robotic system through computer vision and motion control. The microrobotic system showed successful injection results (injecting speed: 15 zebrafish embryos/min) with a 99% success rate, a 98% survival rate. However, both of these

systems require expensive equipment (e.g. AFM and microrobotic system) compared to other methods.
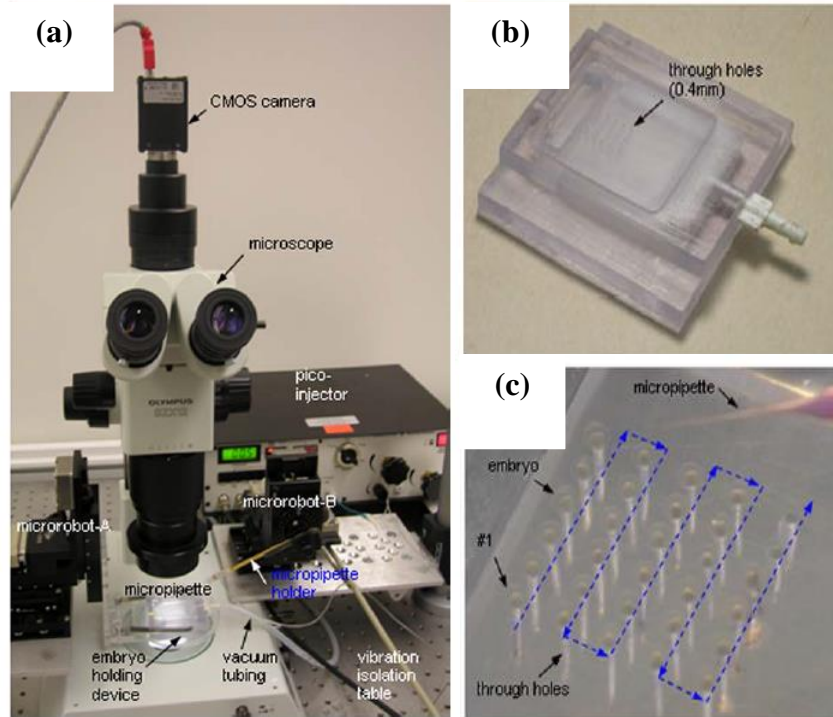
Figure 2.7. (a) Automatic cell injection system. (b) Vacuum-based embryo holding device. (c) An array of trapped embryos with injection path labeled [77].

Microfluidic devices, miniaturized fluid and gas control systems, have developed as a significant tool for various purposes [79]. The microfluidic device integrated with injection systems has shown promise to improve throughput and reduce the potential cell damage by integrating pre- and post-processing operations (e.g. cell culture, sorting, and viability testing) [80]. Microfludics brings various advantages: low cost, reduced sample and reagent volumes, improved portability, high sensitivity, and the potential to be highly automated and integrated to diminish human error [81]. Based on these advantages, microfluidics have been developed in many areas of research in chemistry and biology:

genetic analysis [82], lab on a chip (LOC) or micro total analysis systems (µTAS) [83], [84], cell analysis [85], drug discovery [86], organs on chips [87], and point-of-care (POC) diagnostics [88].

There are a few microfluidic-based microinjection systems already reported in the literature [53], [89]. Ghaemi *et al*. described a novel Polydimethylsiloxane (PDMS)-based microinjection system in a microfluidic format with precise electroosmotic dosage control [53]. As shown in Figure 2.8, a movable microinjection needle (OD: 15 mm, ID: 7.5 mm) is linearly arranged in a straight line with the suction capillary in the channel and electroosmotic dosage control was used to deliver the accurate reagent flow rate (3-14 (pL/s) at DC voltage (5-25 V)). Then, the microinjection needle is inserted into the embryo through deformation of PDMS substrate. They successfully injected Methylene blue solution into the embryo by applying a 25 V for 10 s. Their injection mechanism is simple, and high-throughput microinjections are possible.
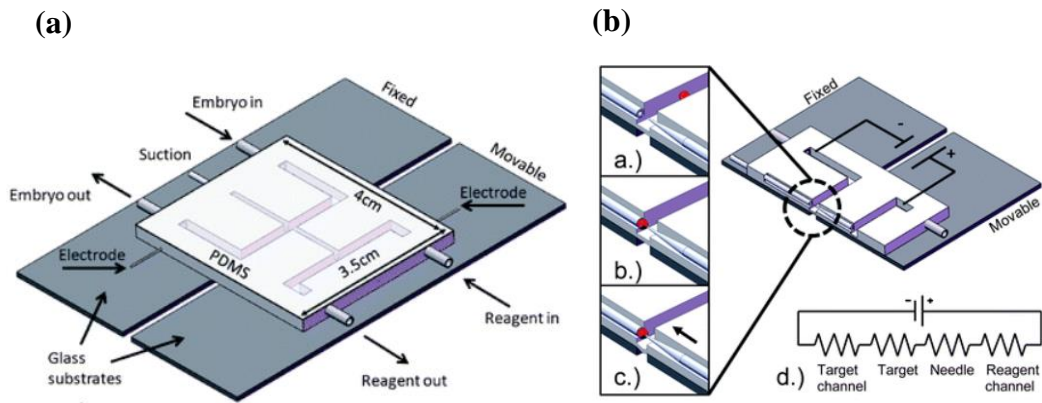
Figure 2.8. (a) Schematic and (b) operation process of the microinjection device with a movable needle [53].

Adamo *et al*. reported a high-throughput microfluidic format single cell

microinjection system as shown in Figure 2.9 [89]. The device uses a stationary injection

needle to penetrate a pressurized cell by hydrodynamic pressure and delivers the reagent

into a cell through the injection needle. In operation, two micro valves (V1 and V2) are

used to control the fluid flowing for transporting a cell. First, a cell is loaded into the

microchannel and delivered in front of the microinjection needle by fluid flowing through

valve operation (V1: Open, V2: Closed) (Figure 2.9(a)). Then, the cell is impinged and

the reagent is delivered into the cell through the microinjection needle (Figure 2.9(b)).

After the injection process, the injected cell is released and transported into channel B for

unloading with valve operation (V1: Closed, V2: Open) (Figure 2.9(c)). They used Hela

cells for their experiment. They successfully visualized the injection process by

introducing ~2.5 (pL) of a fluorescent maker. This approach is very promising for human

cell transfection.
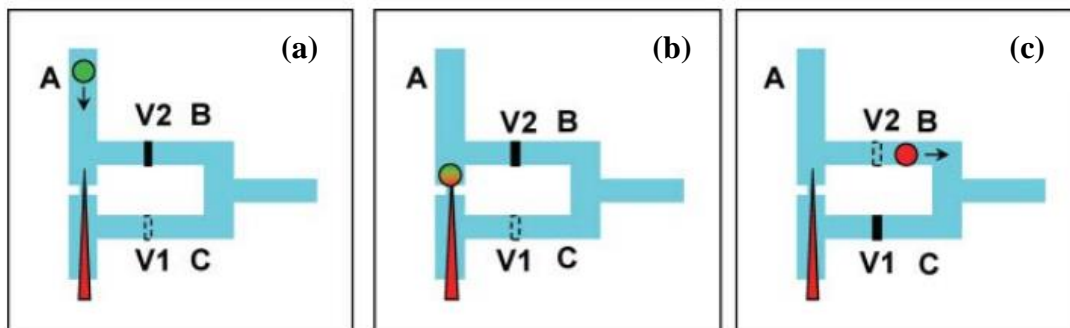
Figure 2.9 Schematic of the microfluidic based single cells micro injection [89].

However, these microfluidic-based transfection devices are designed for human

cell transfection and are not simply applicable for microinjection on mosquito embryos.

There has been no research done to develop a microfluidic microinjection system

specifically for mosquito embryo transfection. The gold standard of mosquito embryo transfection is the manual capillary microinjection method. As mentioned earlier, the capillary microinjection method is, in general, a very labor-intensive method with a low throughput and a high operator skill dependence which hinders the research progress on mosquito embryo transfection-based vector control to reduce mosquito-borne diseases. Mosquito embryos have different shapes and the transfection for mosquito embryos cannot be done randomly like human cells. The injection must be performed on a specific end of mosquito embryos (the posterior pole). This thesis mainly focuses on developing a design and fabrication processes for a low-cost microfluidic system for *Cx. pipiens* embryo microinjection. To create a rather complex microfluidic system integrating microfluidic channels, valves, and microneedles without complicated and expensive micro/nano fabrication processes, and to also lower the overall cost, a 3-D printer is used to fabricate the device. While the device developed through this research is mainly for mosquito embryo transfection, it is anticipated that the 3-D printer-based fabrication technique can be more widely applicable for other microfluidic-based cell or tissue transfection devices.

CHAPTER THREE

3D printed Technology Combined Microfluidic Injection Device

Polydimethylsiloxane (PDMS) has been widely used for microfluidic devices due to several advantages such as its low-cost, biocompatibility, optical transparency, and ease of fabrication. As shown in Figure 3.1, PDMS consists of carbon, silicon, and alkane and has variations in flexibility and adhesion depending on the mixing ratio between the PDMS base and the curing agent [90]. PDMS-based microfluidic devices have been developed and employed for many applications (e.g. protein crystallization, microbial single-cell analysis, cell culture, particle production, and cell microinjection) [91]–[99]. To fabricate PDMS-based microfluidic devices, photolithography and soft lithography are utilized. Photolithography is usually used to fabricate a mold master [100]. Soft lithography, then replicates the mold master, commonly using PDMS.
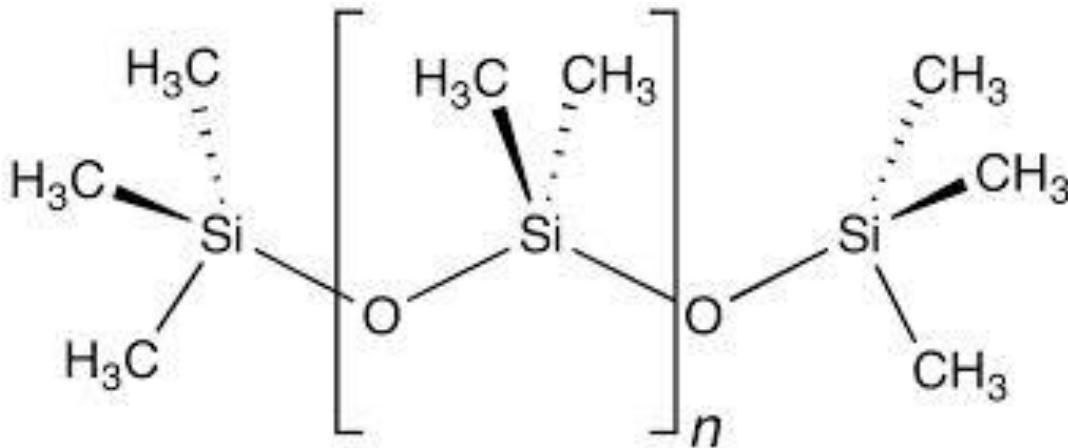
Figure 3.1. Polydimethylsiloxane (PDMS) structural formula [90].

While the photolithography process is simple and straightforward, it still has few limiting factors. Photolithography still requires multiples steps using various chemicals in a cleanroom environment. Moreover, photolithography is unsuitable if the mold master structure has a complex design in the vertical direction. The mosquito embryo has very unique structure as shown in Figure 3.2. The mosquito embryo has an asymmetric elliptical shape, with a length of $750 \pm 20 \, \mu m$ and the widest width of $188 \pm 8 \, \mu m$. The tapered end of the embryo is called the embryo's "posterior pole," where the presumptive germ cells will generate [101]. Germline stem cells are defined by their capacity to self-renew and to generate daughters that differentiate into one or more terminal cell types [102]. Primordial germline stem cells in *Drosophila* start their lives as pole cells, which are products of the first cellularization event in the syncytial embryo. Pole cells are devoted to the germ cell fate at the their formation time through the cytoplasmic inheritance of maternally deposited pole plasm, or germplasm, which is sufficient for germline determination [103]. To suppress the mosquito-borne diseases, germ-line transformation has been used to produce genetically modified mosquito by manipulating the mosquito genome [104]. The transgene-containing DNA must be deposited in the embryo posterior to aid DNA incorporation into the presumptive germ cells [101]. The end of a *Cx. pipiens* embryo, leaned to one side, is observed in Figure 3.2 (Side view). To accurately position the embryo with respect to the injection needle in the microfluidic channel, it is necessary to build a structure that matches with the shape of the posterior of the embryo at the injection location to guide and hold this posterior side of the embryo. However, conventional photolithography process is not adequate to build such a structure

26

Top view **Posterior**	Side view
• Length : 750 ± 20 μm	• Width : 188 ± 8 μm
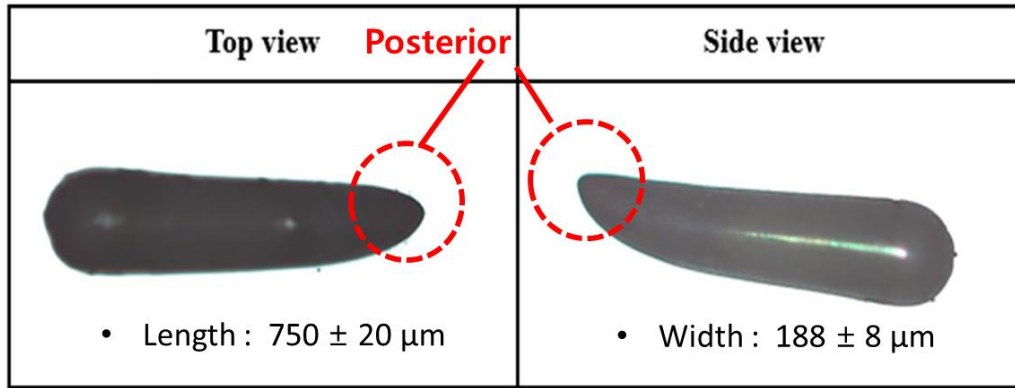
Figure 3.2. Microscope image (top view and side view) of *Cx. Pipiens* image.

Recently, 3D printing has received much attention as a new tool to fabricate microfluidic devices [105]–[111]. With 3D printing, microfluidic chips can be produced in a single step without expensive and complicated microfabrication processes in a cleanroom environment [108]–[111]. Fused Deposition Modeling (FDM), Stereo lithography Apparatus (SLA), and Digital Light Processing (DLP) based 3D printers are commonly used for microfluidic device fabrications. Schematics of them are shown in Figure 3.3.
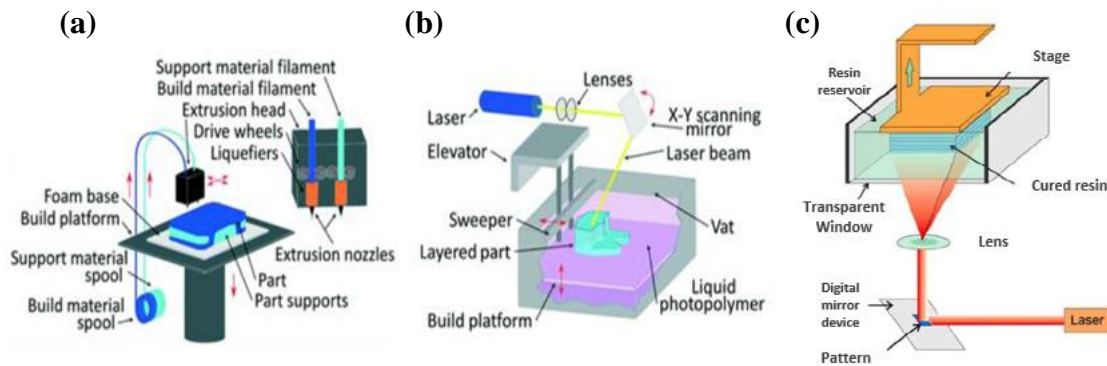
Figure 3.3. Different type of 3D printer (a) Fused Deposition Molding (FDM). (b) Stereolithography Apparatus (SLA) (c) Digital Light Processing (DLP) [99], [130].

For a FDM 3D printer, the extruder heats the material and deposit it layer-by-layer from the bottom to build an object. It has a resolution of >100 μm and thermoplastic such as Polymethyl methacrylate (PMMA) is often used with a FDM 3D printer for microfluidic devices. For an example, Romanov *et al*. demonstrated the use of a FDM 3D printer for microfluidic devices to generate droplets and to track and identify DNA [112].

SLA and DLP 3D printers use liquid photosensitive resins. A SLA 3D printer employs a laser to cure the liquid resin in the tank and build an object layer by layer while a DLP 3D printer exposes the entire layer at once using a beam projector under the resin tank to print an object layer by layer. DLP and SLA 3D printers typically have a higher resolution (resolution > 20 μm) than a FDM 3D printer. Beauchamp *et al*. developed a custom DLP-SLA 3D printer to fabricate a microfluidic device with small dimensions (ridge width: ~30 μm, trenche width: ~20 μm) [113]. They also demonstrated microfluidic particle traps using their SLA 3D printer. Rogers *et al*. reported microfluidic devices with 3D printed control champer and membrane [111].

The DLP 3D printer has especially great potential to be used for microfluidic device fabrication in conjunction with PDMS due to many advantages such as a high resolution, a fast printing speed, and a smooth printed surface. It can also be used to fabricate a mold master for PDMS soft lithography with complex structures that conventional photolithography cannot easily produce.

To fabricate a microfluidic system for *Cx. pipiens* embryo microinjection, we chose a DLP 3D printer (B9 creator 1.2v, B9Creations, USA), as shown in Figure 3.4, to print the mold master for PDMS. The 3D printer has 30, 50, or 70 μm XY resolution and

its vertical resolution is dependent upon the type of resin. Five different resins are available through the manufacturer, while the 3D printer is open to third party resins. We chose the manufacturer's black resin (minimum Z resolution: 30 μm) to print the mold master because black resin showed less thermal deformation comparison of other resins during PDMS curing process.

Figure 3.4. Digital Light Processing (DLP) 3D printer (B9creator 1.2v).

Understanding of the precision and the accuracy of 3D printers is important to successfully build the mold structure of a microfluidic system for *Cx. pipiens* embryo microinjection. Precision means consistency in dimensions of 3D printed structures [114]. Accuracy is determined by how close a printed structure dimension is compared to a target value. To determine the precision and accuracy of the DLP 3D printer, we

29

performed experiments using test devices which contains microchannel structures with various lengths and dimensions.

Figure 3.5 shows the test device used for precision analysis for the different lengths. Microchannels with three different lengths (1 cm, 2 cm, 3 cm) were triplicated to see the repeatability. The height and width of the channel structures were measured at the location indicated in the figure and compared.
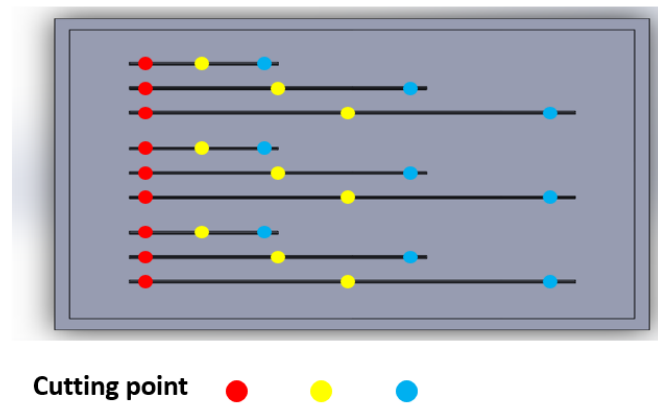
Figure 3.5. Top view of microchannel sample and cutting points for precision analysis of 3D printed microchannels.

While the measured height and width show pretty consistent results, it is found that the printed height and width differ from the design parameters. Also as shown in Figure 3.6, the printed microchannel shape (Figure 3.6 (b)) is not symmetric as anticipated. An ideal shape of the microfludic channel for the microfluidic-based microinjection device for mosquitoe embryos is shown in Figure 3.6 (a). The microchannel has to be symmetric with rounded corners for proper microfluidic valve operation to control the fluid flow without leakage. And its height and width dimensions must be close to 200 µm which is slightly bigger than the average size of mosquito embryos to effectively transport the embryo inside the microchannel. To determine the

optimum design parameters, that produce the width and height of 200 µm, and the

optimum correction structure added on one side of pattern to achieve symmetric channel

geometry, another test structure was designed and tested.
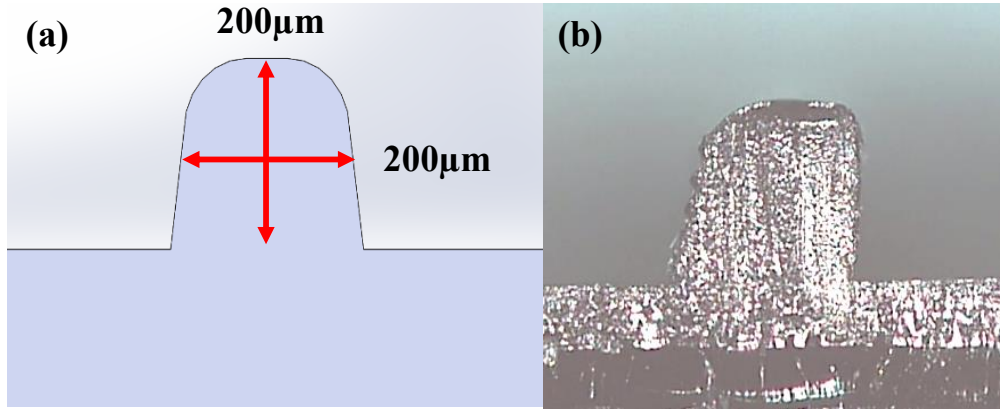
Figure 3.6. Cross section view of microchannel showing (a) ideal shape and (b) actual shape with asymmetry.

The test structure to determine the optimum design parameters and the optimum

correction structure is shown in Figure 3.7. There are 9 rows with different height and

width and, in each row, there are 6 different correction structures as shown in Table 3.1.

The definition of the correction structure with repect to the assymetric printed structure is

shown in Figure 3.7(b). The length of the channels was kept constant to be 4 mm. In

order to test the influence of temperature, we tried two different temperature (25°C and

40°C). Before printing, the black resin was shaken for 6 minutes on an orbital shaker at

160 rpm and then heated in a water bath. The water temperature was monitored with an

infrared temperature gun. The heated resin was then poured into the DLP 3-D printer vat

and printed. The printed structures were rinsed with DI water and Isopropyl alcohol

(IPA), and dried with a nitrogen gun. Then, the molds were cured for 30 seconds in the

resin curing box.
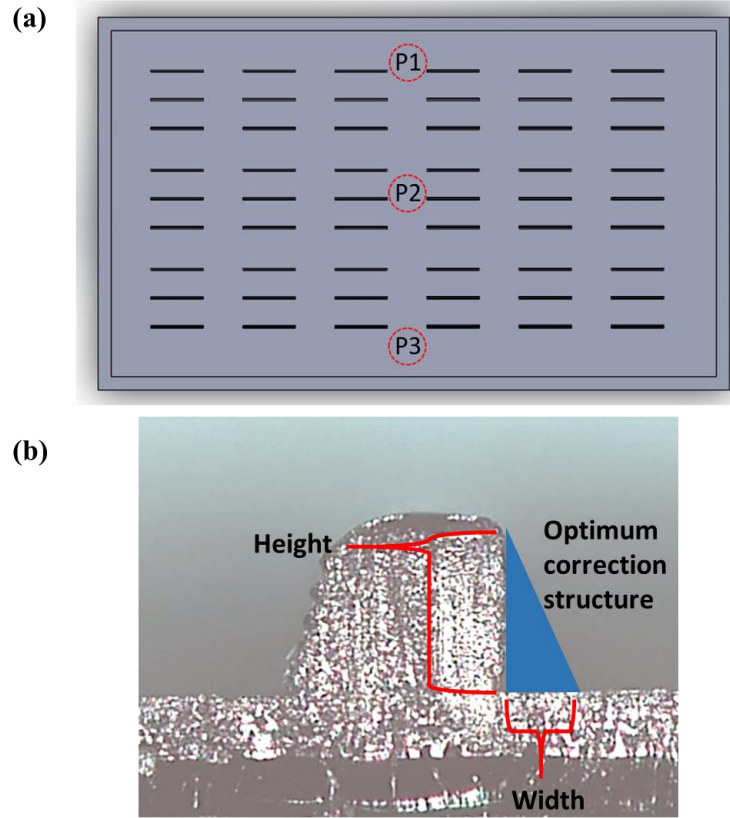
Figure 3.7. (a) The 3D-printed test model, including microchannels with various dimensions and error correction structures. (b) Optimum correction structure.

Table 3.1. Microchannels design dimension and error structures dimension.

Microchannel dimension	Height (µm)	Width(µm)	Correction structure dimension	Height(µm)	Width(µm)
1	240	120	1	120	30
2	240	150	2	120	60
3	240	180	3	150	30
4	270	120	4	150	60
5	270	150	5	180	30
6	270	180	6	180	60
7	300	120			
8	300	150			
9	300	180			

Figure 3.8 shows the measurement results. For both height and width, the red solid line indicates the design parameter. Data above the red line means the measured dimension from the fabricated test structures is larger than the design parameter while data below the red line indicates the measured dimension is smaller than the design parameter.
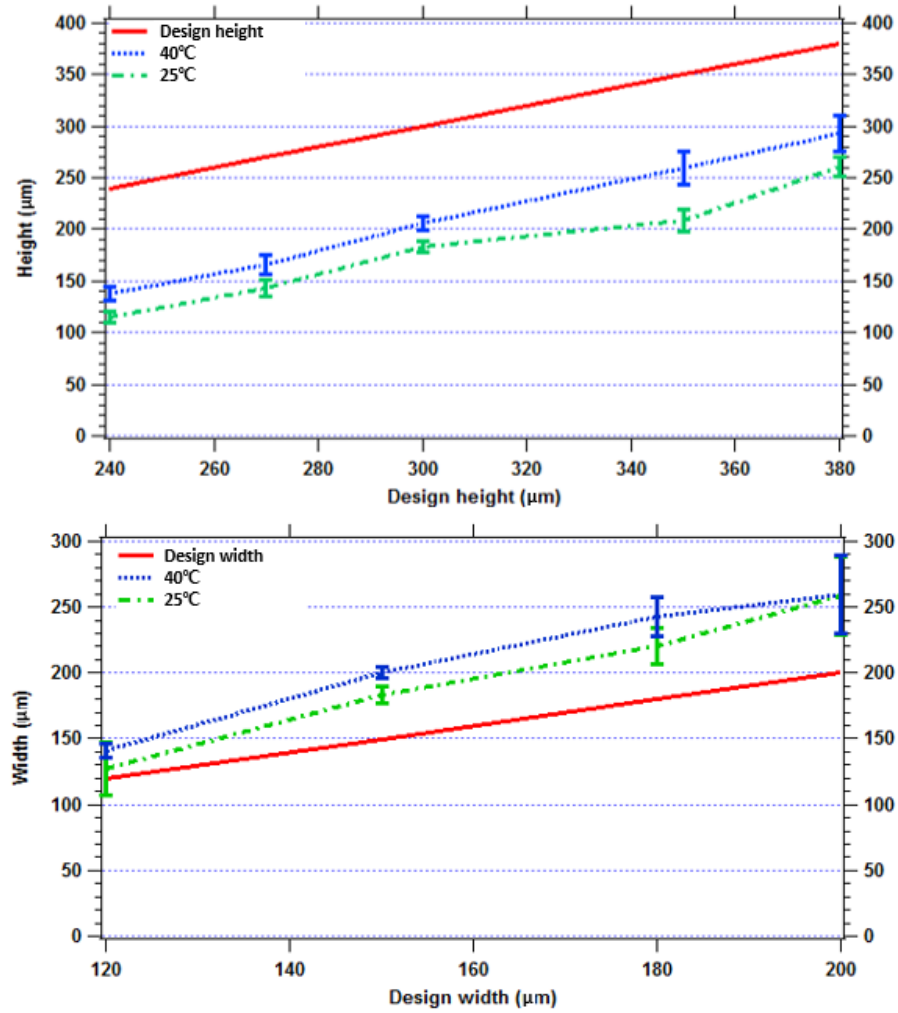
Figure 3.8. Comparison of design parameter and actual printed microchannel dimension with 25°C and 40°C resin temperature. (a) Graph of printed height versus design height. (b) Graph of printed width versus design width.

For both printing temperatures, measured width and height increase reasonably linearly as the design parameter increases. Also, the dimension printed at 40°C shows slightly bigger than that at 25°C for both height and width. The largest standard deviation of measured results for width was 257 ± 30 µm at 25°C, when the designed width was 200 µm. For height, the largest standard deviation was 258 ± 16.9 µm at 40°C when design has a height of 350 µm. Considering the DLP 3D printer used has the XY resolution of 30 µm and the Z resolution of 30 µm for the black resin, these standard deviations are less or equal to the resolution. For the design height of 300 µm and the design width of 150 µm at 40°C, the 3D printed structure has a measured height of 206 ± 6.3 µm and a measured width of 200 ± 4.2 µm which are close to the ideal microchannel dimensions. So we were able to determine the optimum design parameters to be 300 µm for the height and 150 µm for the width. For these parameters, we were able to determine that the optimum correction structure to be 180 µm for the height and 60 µm for the width. The cross-sectional view of the final opimized structure with these design dimenions is shown in Figure 3.9.
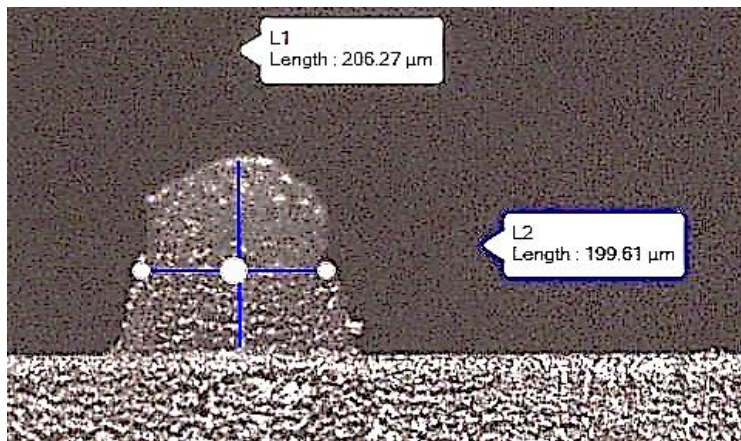
Figure 3.9. Cross-section view of the final optimized structure with 40°C (design parameter: 300 µm height and 150 µm width) with the optimum correction structure (height: 180 µm, width: 60 µm).

Additionally, we measured the surface roughness at P1, P2, and P3 in Figure

3.7(a) using an Atomic Force Microscope (AFM). A 30 µm x 30 µm area was scanned at

each point and analyzed. Figure 3.10 shows the surface roughness measurement results.

For the structure printed at a temperature of 25°C, the measured root mean squared

(RMS) roughness was 84.7 ± 22 nm. The roughness (100.97 ± 16 nm) increases slightly

at 40°C, but the difference is minor. So finally, we concluded the optimum design

parameters are 300 µm for the height and 150 µm for the width and the optimum

correction structure is 180 µm for the height and 60 µm for the width at the printing

temperature of 40°C.
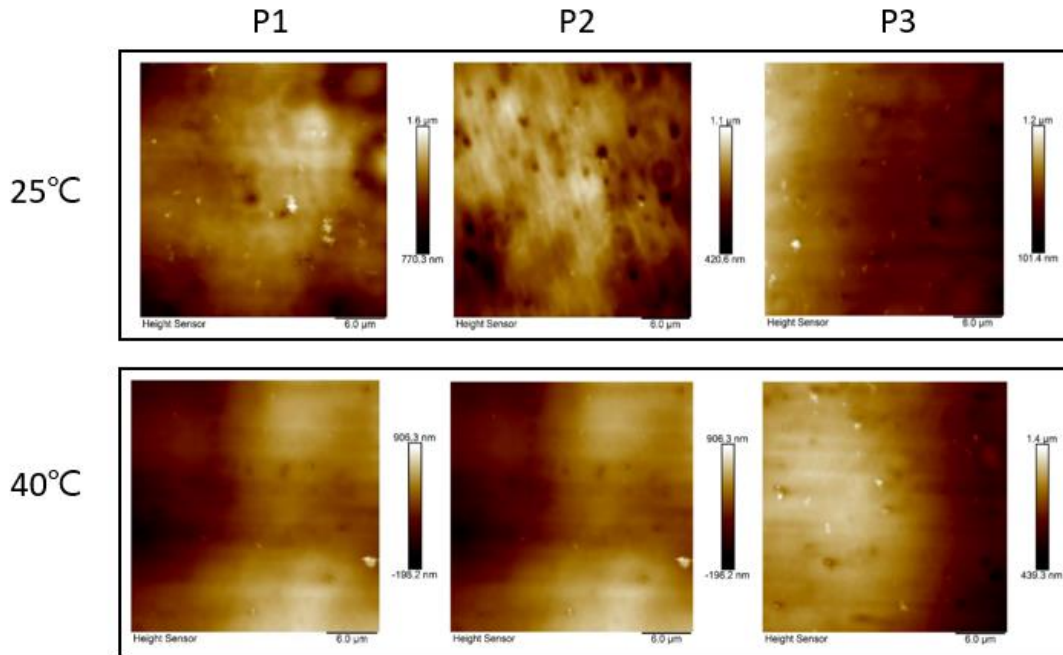
Figure 3.10. Atomic Force Microscope (AFM) images of the 3D-printed PDMS mold
masters with different resin temeprature (25°C, 40°C) at different points.

As discussed earlier, it is important to build a guide structure that matches with

the embryo's posterior. As shown in the Figure 3.2, the posterior side of the embryo has

an angle of 27° horizontally and 20° vertically. The potential guide structure for the

consideration must have an angle slightly larger than the largest angle of the embryo's posterior which is 27° in all directions. Otherwise, if the angle of the guide structure is smaller than this, the posterior side of embryo may not be properly positioned in it. Or if the angle is too big, then the posterior side of the embryo may be away from the needle which makes it difficult to accurately inject the needle. To determine the optimum design paramters for the guide structure, a test structure is designed as seen in Figure 3.11. The test structure has a straight channel part and angled structures with different angles in both horizontal and vertical directions at the end of it. To investigate the consistency of printed angle accuracy, there are nine identical structures for each angle. The optimal design parameters and correction structure determined earlier are used for this design. Six different angles from 10° to 60°, with increments of 10°, are designed as shown in Figure 3.11 (b). Table 3.2 outlines the detailed design parameters. The horizontal angles of the fabricated structure are measured from the top view of the structure while the printed test structure was cut into multiple pieces with a razor blade to measure the vertical angles from the side.

Table 3.2. Taper structure design parameter.

Angle(degree)	Desired height (µm)	Design Height (µm)	Design length (µm)
10°	200	300	1700
20°	200	300	820
30°	200	300	520
40°	200	300	360
50°	200	300	250
60°	200	300	170
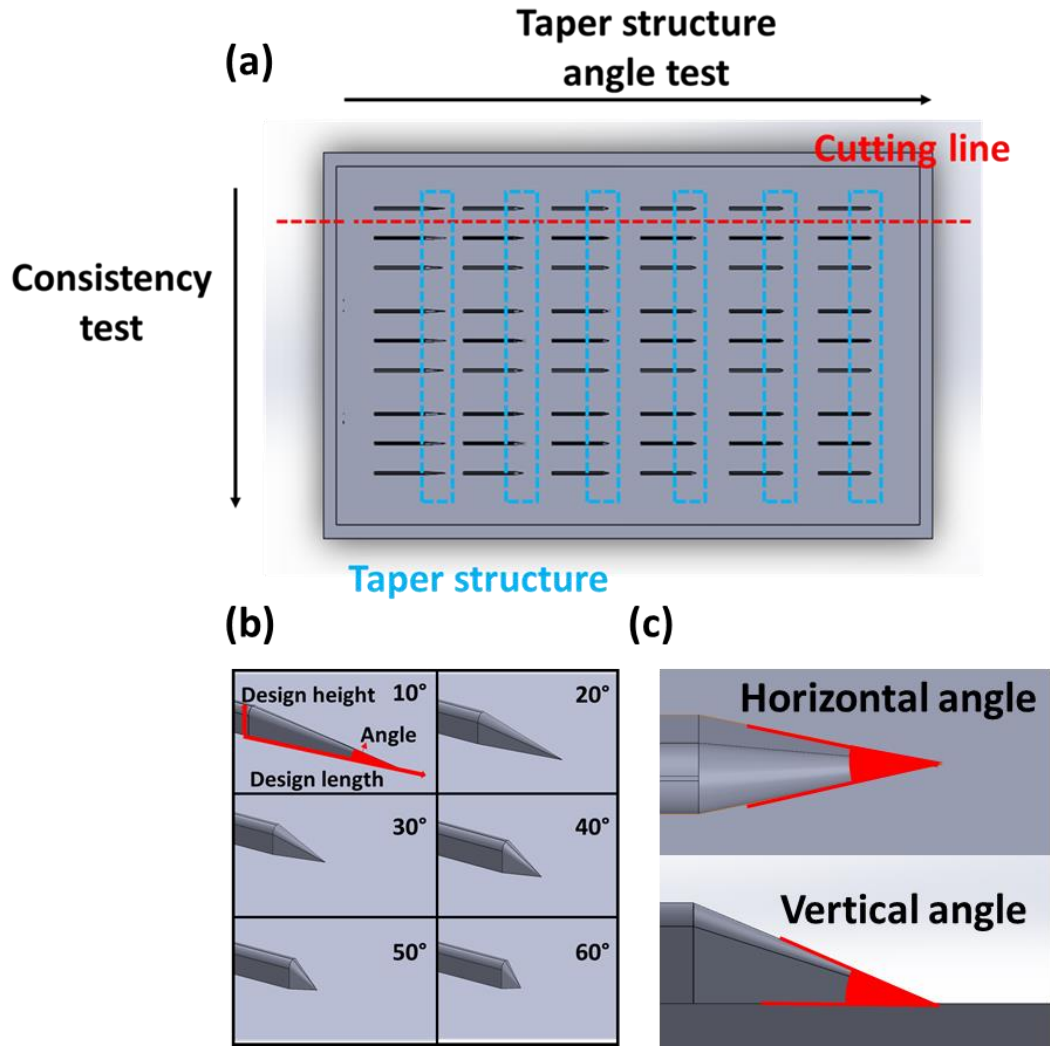
Figure 3.11. (a)The 3D-printed PDMS mold master with taper structure showing cutting line for measurement. (b) Different taper structure image with various full angles (from 10° to 60° with an increment of 10°) (c) Measuring angles in horizontal and vertical plane.

Figure 3.12 shows the microscope images of the printed test structures. The staircase-like structure was observed which is obviously due to the layer-by-layer printing method. However, we believe it will not affect the functionality of the structure to guide the mosquito embryos. If necessary, a polishing technique, such as an acetone bath, may be employed to smoothe the surface. The measurement results are shown in Figure 3.13. The red line in the graph indicates the designed angle. The angle in

horizontal direction shows slightly larger angle compared to the design (design angle +1.8 ± 1.7°) while the vertical direction angle is slightly smaller than the design (design angle – 2.14 ± 0.9°). Since the horizontal and vertical angles can not be independently controlled, the final design angle is determined to be 30° so that the angle of the tapered structure in either direction to be as close as possible to 27°. Note that this result shows the clear benefit of 3D printing for this device fabrication. It might be very difficult to produce this shape of structure with a conventional photolithography process while we were able to fabricate this with 3D printing with a single step process.

Figure 3.12 Actual printed taper structures microscope image at top and side view.
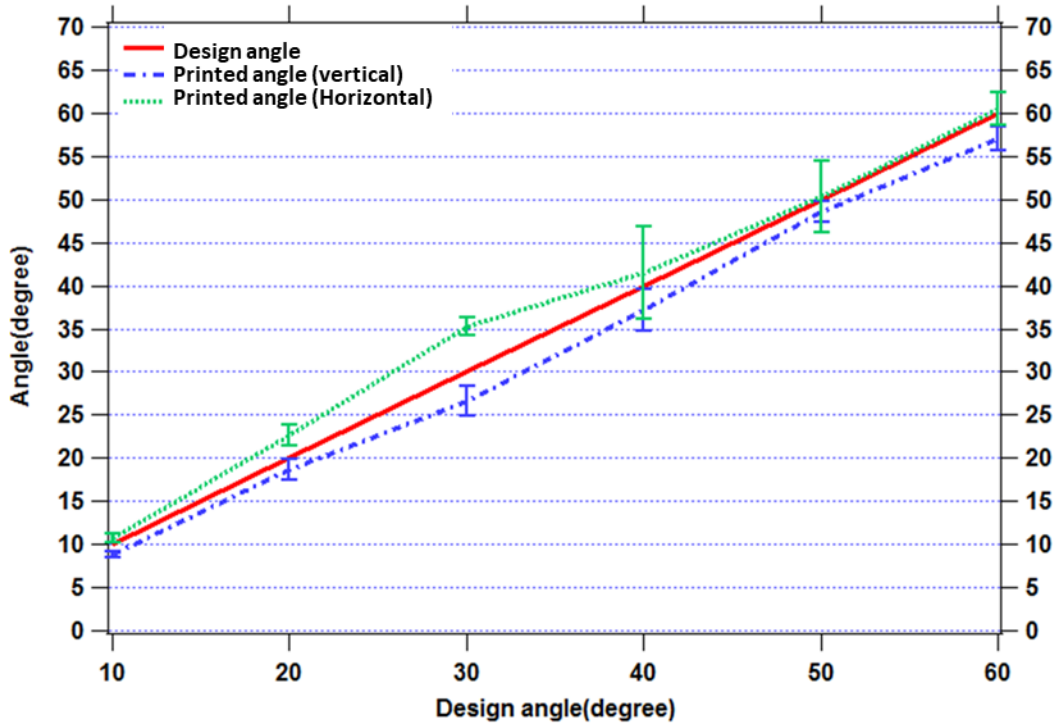
Figure 3.13. Graph of design taper structure angle vs actual printed taper structure angle with 40°C resin.

In conclusion, we were able to completely characterize the DLP 3D printer and determine the optimum design parameters to fabricate microchannels with target dimensions (height: 200 µm, width: 200 µm), the optimum correction structure to make the channel symmetric, and the optimum design parameters for the embryo's posterior guide structure. In the next chapter, we are going to discuss about the details of the fabrication process of a microfluidic system using all these design parameters.

CHAPTER FOUR

Fabrication and Demonstration of a Microfluidic Device toward a Microfluidic
Microinjection System for *Cx. pipiens* Embryos

A microfluidic-based microinjection device for *Cx. pipiens* embryos is designed
as shown in Figure 4.1 using the design parameters determined from chapter 3. It consists
of the PDMS top part and the 3D-printed bottom part. Two pneumatic valves with a
syringe pump are used for the embryo transportation and injection. Inlet and outlet ports
are designed to be bigger than the diameter of Tygon tubing (OD: 0.078") through which
mosquito embryos will be loaded and unloaded. Tygon tubing will be attached to inlet
and outlet ports using an epoxy glue. The inlet port tapers down to the microfluidic
channel to ensure proper transfer of embryos into the channel, which has a height and
width of 200 μm (design parameter: height of 300 μm and width of 150 μm). As
described in chapter 3, the microchannel dimension is slightly bigger than the size of *Cx.
pipiens* embryos for proper transport. The microfluidic channel is tapered down again in
front of the glass capillary needle tip with an angle that matches with the shape of the
mosquito embryo's posterior side as described in chapter 3. There is a bypass channel
(channel height: 60 μm , width: 60 μm) connecting this tapered end to the output
microfluidic channel so that the fluid is allowed to flow for delivering the embryo to the
needle tip while the embryo cannot pass through. The microfluidic channel towards the
outlet port has a slightly wider width (250 μm) with the same height of 200 μm, for easy
unloading of injected embryos. A taper structure is employed again to connect this
channel to the outlet port.
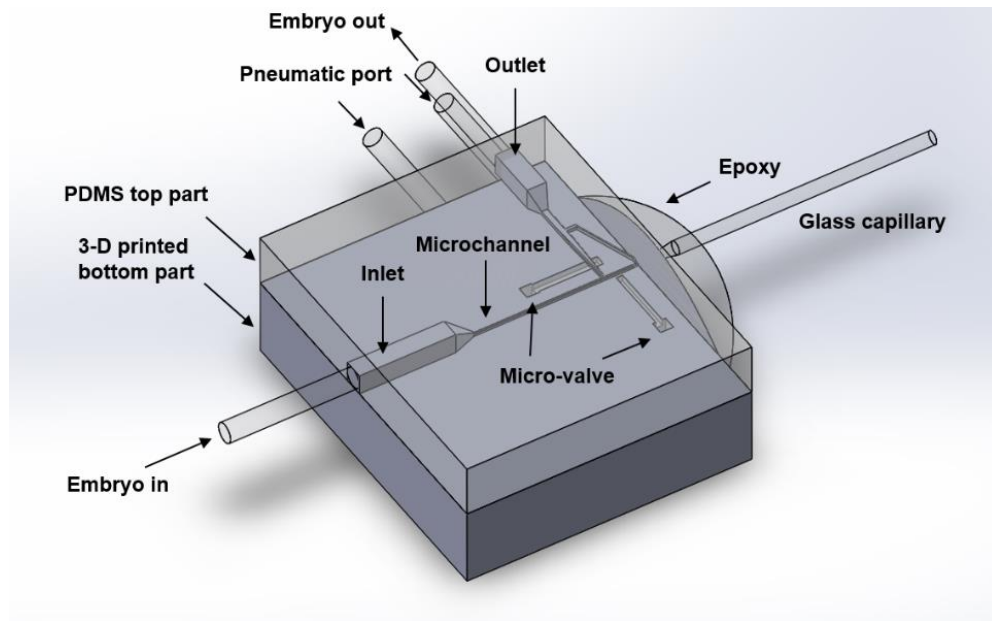
Figure 4.1. The schematic drawing of a microfluidic-based microinjection device.

The detailed operation procedure of this microfluidic microinjection device is presented in Figure 4.2. A mosquito embryo will enter into inlet from embryo supply reservoir and move to the injection location C1 as seen in Figure 4.2(b) (Syringe pump direction: forward, valve 1 (V1): closed, valve 2 (V2): open). The loaded embryo will be observed under a microscope. The injection step will be performed by pressurizing a mosquito embryo in the microchannel with a syringe pump. After embryo injection is complete, the embryo will be unloaded through the outlet through valve control. Once the injection process is successfully completed, the injected embryo will be pulled back from the glass needle and move to C2 (Figure 4.2(c), Syringe pump: reverse, V1: closed, V2: open) in the microchannel. Finally, the embryo will unload through the outlet (Figure 4.2(d), Syringe pump: forward, V1: open, V2: closed).
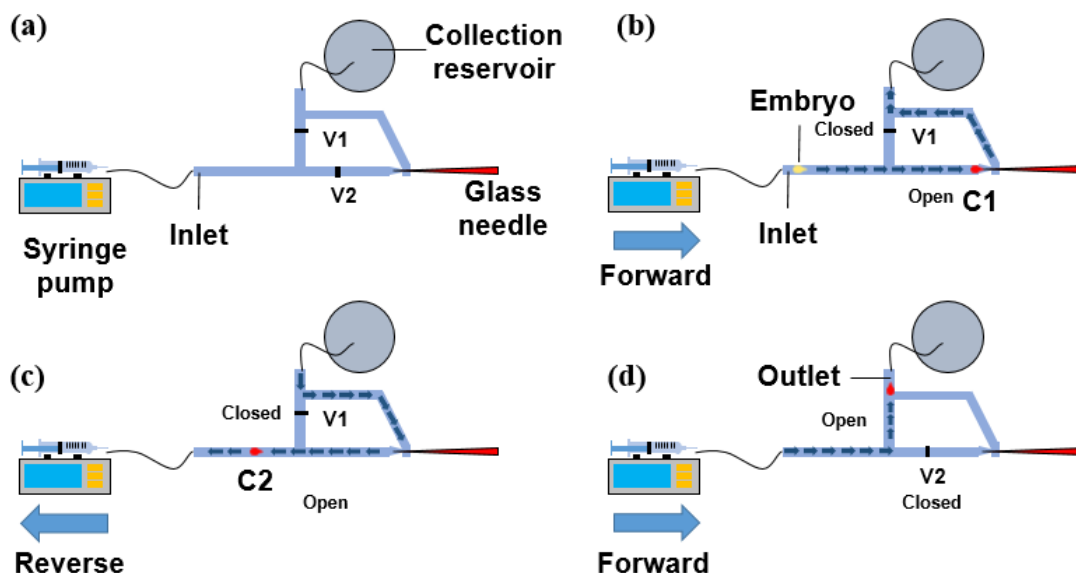
Figure 4.2. The schematic representation of design and operation of a microfluidic-based microinjection system for *Cx. pipiens* embryos.

Before attempting the microinjection on *Cx. pipiens* embryos with the microfluidic device, it is necessary to develop its complete fabrication process, demonstrate the functionality of the valves with external pneumatic controls for the fluid flow control, and inspect the behavior of a *Cx. pipiens* embryo in the microfluidic channel. This is the main objective of this thesis, to lay the foundation for a fully functional microfluidic-based microinjection device.

The unique aspect of the proposed microfluidic microinjection device is the use of both 3D printing and PDMS. Because of the many attractive benefits of 3D printing and PDMS, there has been growing interest in developing microfluidic devices by integrating 3D-printed structures with PDMS in order to take advantage of both. For example, Gross *et al*. reported the design and fabrication of a 3D-printed microfluidic device for cell lysis [115]. For their device, PDMS is coated on 3D-printed device to avoid effects of unknown surface properties of a commercial 3D printing resin. Brennan *et al*. reported an

SLA 3D-printed device integrated with gas permeable PDMS membranes to control oxygen levels for cell cultures [116]. Using a reversible bonding method with a thin intermediate PDMS layer, PDMS membranes were attached to 3D-printed parts. Tsuda *et al*. fabricated a flow selector device by using PDMS and a FDM-based 3D printer [117]. The PDMS membrane valve was chemically bonded to the 3D-printed structure using APTES.

One key challenge in the integration of PDMS and DLP-printed structures is achieving a strong bond between the two. Since most of DLP resins are proprietary and chemical compositions are unknown, it is difficult to directly use the bonding techniques used for PDMS with other traditional substrates. Therefore, it is necessary to experimentally find the best bonding techniques. Based on various reported techniques, we investigated five different intermediate layers: double-sided tape, a PDMS/tape composite, UV glue, (3-Aminopropyl) triethoxysilane (APTES), and sputter-deposited SiO_2. To test the bonding strength between PDMS and the DLP 3D-printed part, we designed a simple burst test structure as shown in Figure 4.3. The same DLP 3D printer used for chapter 3 (B9 creator 1.2v, B9Creations, USA) was also used to print the mold master for PDMS top parts and 3D-printed bottom parts that contain a pneumatic port. We chose the black resin to print the mold master and the yellow resin (minimum Z resolution: 20 μm) for the 3D printed component of the burst test structure.

BURST TEST STRUCTURE
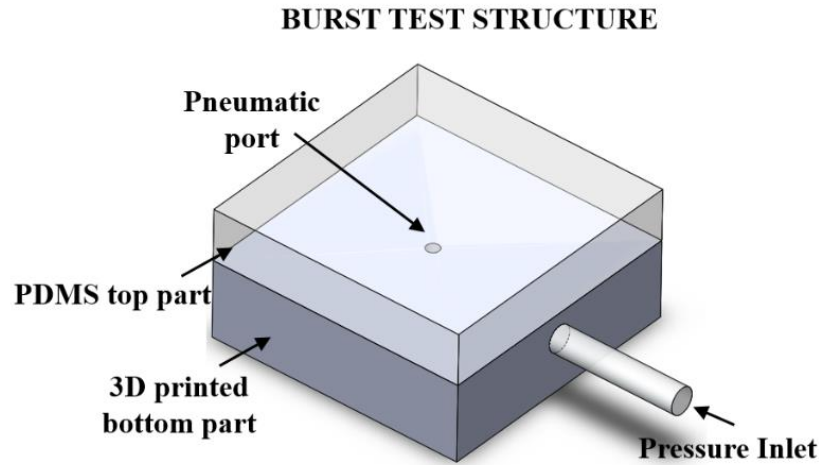
Figure 4.3. Schematic of a burst test structure.

Figure 4.4 shows the fabrication process of the burst test structure. To create a PDMS top part with a 3D printed mold master, we used soft lithography processes. The 3D printed PDMS mold master has an inner dimension of 25 mm (width) x 50 mm (length) x 4 mm (height). It was treated with Trimethylchlorosilane (TMCS) (SIGMA-ALDRICH, USA) before PDMS molding. TMCS treatment was performed in a desiccator with an opened TMCS bottle. TMCS molecules cover the mold surface and prevent PDMS from sticking to the mold. First, the SYLGARD 184 Silicon elastomer was mixed thoroughly at a 1:10 (curing-agent: base) weight ratio. Subsequently, the mixed PDMS was put into degassing chamber to remove micro-bubbles for 1 hour 30min at -100 kPa. Then, as shown in Figure 4.4 (a), the degassed PDMS was poured on the 3D-printed mold master (Steps 1-2) and cured in an oven at 65°C for 2 hours. After curing, the PDMS piece was cut along the edge of the mold and gently peeled off from the mold master. Finally, the molded PDMS was cut into 2 cm x 2 cm pieces to produce two PDMS top parts.
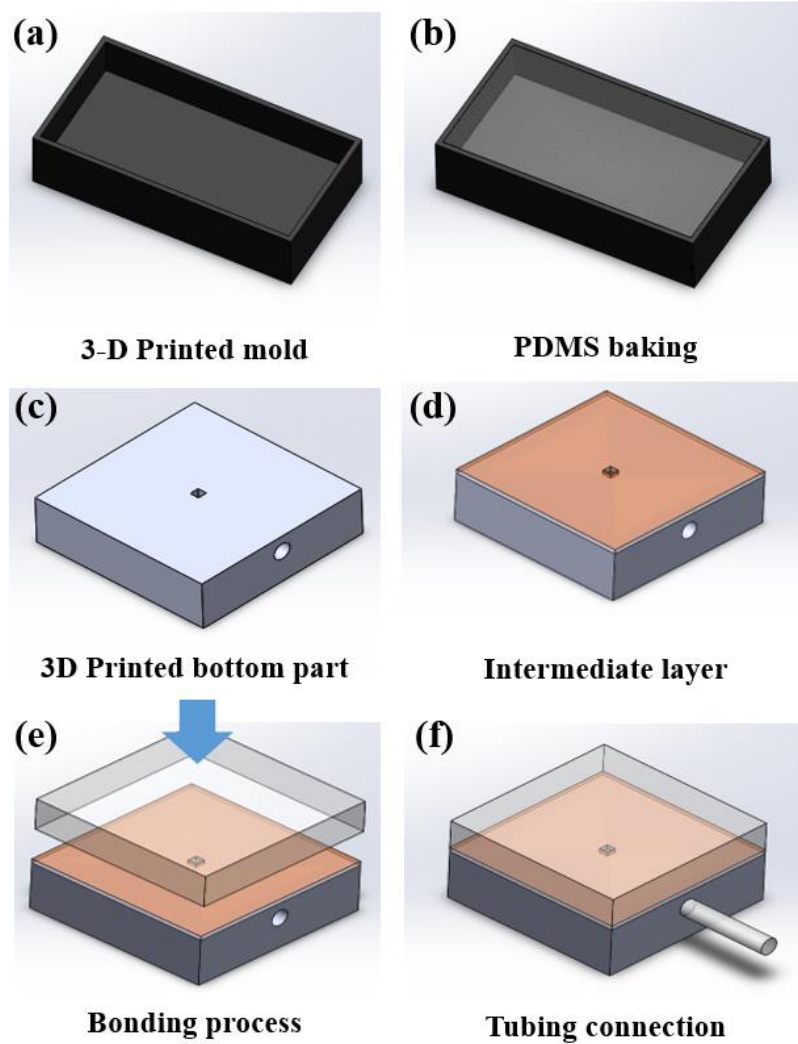
Figure 4.4. Fabrication process of the PDMS/Intermediate layer/3D-printed bottom part. (a) Printing the PDMS mold master. (b) PDMS baking. (c) Fabricating the 3D-printed bottom part using DLP 3D printer. (d) Intermediate layer on top of the 3D printed bottom part. (e) Bonding process of the top PDMS part/3D printed bottom part with an intermediate layer. (f) Connecting a Tygon tubing to the burst test structure.

As shown in Figure 4.4 (c), the 3D printed bottom part contains a pneumatic port (1 mm in diameter) and inlet (2 mm in diameter). After printing, 3D printed parts were rinsed with DI water and IPA to remove residues, followed by nitrogen drying. The intermediate layer to be tested was then applied to the 3D printed part for the bonding strength experiment as seen in Figure 4.4(d).

Double-sided tape is the simplest form of an intermediate layer for bonding. It has been used to adhere PDMS to glass for micro particle image velocimetry (PIV) measurement devices [118], PDMS to PMMA for a microfluidic device for the observation of perturbation of Drosophila embryos [119], and PMMA to PMMA for droplet formation devices [120]. In our experiment, double-sided tape (3M Double Coated Tape 444, 3M Corp) was simply attached to the surface of a 3D-printed bottom part and the pneumatic port was cut out using a scalpel. A PDMS top part was gently placed on the tape and pressure was applied to remove trapped air pockets between the PDMS and tape. Then, the burst test structure with double-sided tape was baked at 65°C for 2 hours to increase its bonding strength. During the baking process, the burst test structure was sandwiched between two flat plastic plates and a 300 g weight was placed on top of it to apply uniform pressure.

PDMS/tape composites have also been used to bond PDMS to different materials. Kim *et al*. reported the use of it to bond PDMS to various substrates (e.g. PDMS, glass, plastic, and silicon) for a microfluidic channel, reactor, microfluidic system-integrated membrane, and an electrochemical biosensor [121]. In our experiment, to create PDMS/tape composite as an intermediate bonding layer, double-sided tape was first attached to the surface of a 3D-printed part. Then, degassed PDMS, mixed at a 1:10 (curing agent: base) weight ratio, was spin-coated onto the tape at 3150 rpm for 1 minute. After waiting for 15 minutes, the PDMS was then heated in an oven at 65°C for 18 minutes to produce a partially-cured PDMS layer with a thickness of 20 μm. The pneumatic port area of the partially-cured PDMS/tape composite was carefully cut and removed. A PDMS top part was then gently placed on the PDMS/tape composite and

pressurized to remove air pockets. Finally, the burst test structure with a PDMS/tape composite intermediate layer was sandwiched between two flat plastic plates and baked at 65°C for 3 hours. A weight of 300 g was placed on the sample to achieve a uniform and strong bond between the PDMS top part and the partially-cured PDMS layer.

UV glue has been used as an intermediate bonding layer to bond PDMS to PDMS to fabricate microfluidic devices for vancomycin-resistant Enterococcus (VRE) diagnosis and highly effective viral filtering [122], [123]. For UV glue bonding, we used a stamp-and-stick process [124]. A UV glue (NOA 86H) was poured onto a transfer substrate and then spun at 1000 rpm for 3 minutes. Then, the 3D-printed bottom part was brought into contact with the UV coated transfer wafer for stamping. After that, the PDMS top part was placed on the glued 3D-printed part and pressurized. The burst test structure with a UV glue intermediate layer was cured in a UV box for 1 minute.

APTES has been used to bond PDMS to TP (e.g. PC, PMMA and ABS), and PDMS to PS or epoxy-type polymers chemically [125]–[127]. Silanol (Si–OH) groups form on the surface treated with APTES and oxygen plasma-treated PDMS surfaces to achieve irreversible bonding. In our experiment, a 3D-printed part was first treated with oxygen plasma for 1 minute to activate the surface. After plasma treatment, the 3D-printed part was immediately immersed in 5% (volume/volume %) APTES solution at 50°C for 20 minutes. After rinsing with DI water and drying with nitrogen, the APTES treated 3D-printed part and the PDMS top part were treated with oxygen plasma. Then, the treated top and bottom parts were attached. The burst test structure with an APTES intermediate layer was sandwiched between two flat plastic plates and clamped for 1 hour.

47

Sputter-coated SiO$_2$ has been used as an intermediate bonding layer to bond PDMS to PMMA [128]. It was reported that the SiO$_2$ layer thickness should be less than 100 nm to generate a high bonding strength. In our experiment, we deposited SiO$_2$ on a 3D-printed bottom part using a magnetron RF sputterer at a power of 150 W for 13 minutes 30 seconds and an Ar flow rate of 20 sccm. The resulting SiO$_2$ thickness was 77 nm. Then, both the SiO$_2$ surface and PDMS top part were treated with oxygen plasma to activate the surfaces. Lastly, they were attached and the burst test structure with a SiO$_2$ intermediate layer was sandwiched between two flat plastic plates and clamped for 1 hour in a room temperature.

After bonding the top PDMS part to the 3D-printed bottom part with the intermediate layer (Figure 4.4 (e)), Tygon tubing is attached to the inlet using an epoxy (5min epoxy, Gorilla, USA) as shown in Figure 4.4(f). Note that the bottom surface of the PDMS, which was previously contacting the mold surface, is attached to the 3D-printed part.

A schematic of the burst test set up is shown in Figure 4.5(a). Regulated compressed air at 800 kPa was connected to a solenoid valve manifold. The solenoid valve (MHA1-M1LH-3/2G-0.6-PI, Wolf-Solution, USA) was controlled by a controller (CECC-D, Wolf-Solution, USA) through CODESYS to turn the compressed air on or off. A compact compressed air regulator (0-450kPa, McMASTER, USA) was connected to control the pressure applied to the burst test structure. Polyurethane tubing (PU-156F-0, Cole-Parmer, USA) from the compact regulator is attached to a barbed tube (51525K272, McMASTER, USA). The barbed tube, then, was connected to Tygon tubing (inner diameter: 0.02", Cole-Parmer, USA) via a disposable needle (22 gauge, McMASTER,

USA). Finally, the Tygon tubing was connected to the burst test structure through a metal

pin (22RW, New England Small Tube, USA). A microscope (Olympus BX51, Olympus,

USA) was used to monitor changes at the pneumatic port area as we increased the applied

pressure. Figure 4.5(b) shows the actual test set up. Since PDMS is gas permeable, the

pressure inlet of the burst test structure was first filled with DI water. The inlet was then

pressurized at 55.16 kPa (8 psi) for 1 hour to completely remove trapped air from the

pneumatic port through the PDMS. To monitor air leaks coming from the device, a soap

solution was applied. For the burst pressure test, we increased the applied pressure by

6.89 kPa (1 psi) per 1 minute starting from 55.16 kPa until delamination patterns

developed.
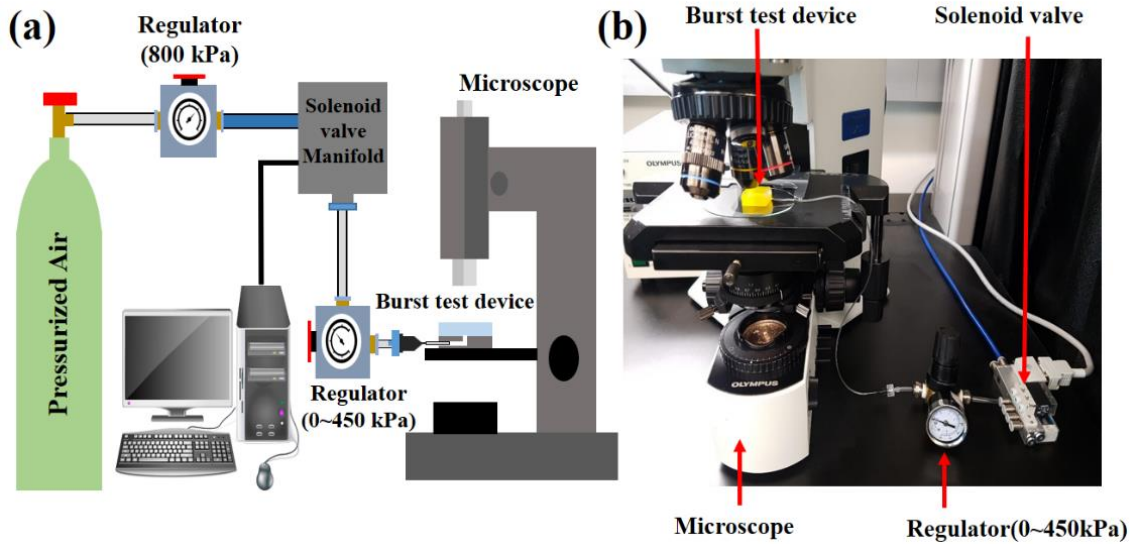
Figure 4.5. (a) A schematic and (b) an actual image of the burst test system setup.

We fabricated three samples for each intermediate layer and measured the burst

pressure at which delamination developed and eventually caused the structure to fail. The

average burst pressures for five different intermediate layers with error bars (± standard

deviation) are shown in Figure 4.6. Figure 4.7(a) shows microscope images of the
pneumatic port area to show delamination progression. Note that the time is not on a
same scale, since the time to failure differed for each bonding method. We also
performed a peel-off test by manually peeling the PDMS from the intermediate layer to
check the bonding state (reversible/irreversible) and those results are depicted in Figure
4.7(b).
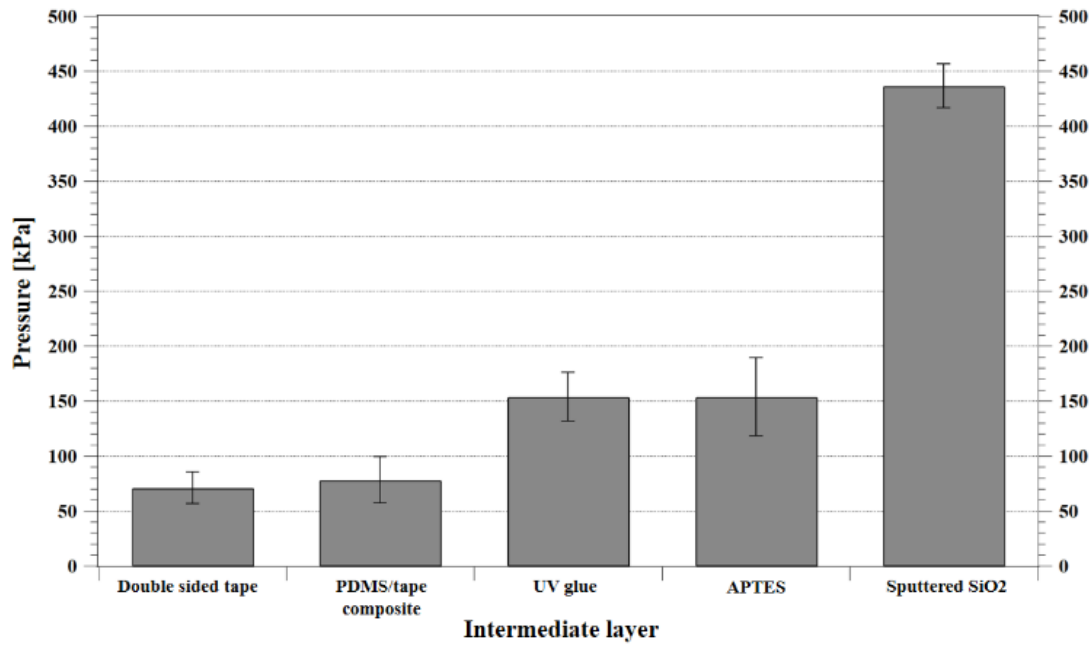
Figure 4.6. A comparison of the burst pressure for five different intermediate layers
(Adhesive tape, PDMS/tape, UV glue, APTES, Sputtered SiO_2).

The double-sided tape and PDMS/tape composite intermediate layers show
noticeably low bonding strengths with an average burst pressure of 71.22 kPa and 78.12
kPa, respectively. Figure 4.7(a) shows the delamination pattern of Saffman-Taylor
fingers [129], [130], which grow over time. It took 3 hours from the formation of these
patterns to complete failure. The PDMS top part was easily separated from the
intermediate layer in the peel-off test, as shown in Figure 4.7(b). Such low bonding

strength and reversible bonding state may be due to the fact that PDMS had not formed a cross-linked bond network with the double-sided tape regardless of PDMS conditions (e.g., fully cured PDMS or partially cured PDMS).

The UV glue intermediate layer provided a stronger bonding strength (burst pressure: 153.96 kPa) than the double-sided tape and PDMS/tape composite. The delamination pattern that developed was a round shape rather than finger shapes as shown in Figure 4.7(a). However, the delamination progressed faster than that of the double-sided tape and PDMS/tape composite. It took less than 1 minute from formation to complete failure. From the peel-off test, we found that the UV glue bond was reversible

The average burst pressure of the structure with an APTES intermediate layer was 153.93 kPa. As shown in Figure 4.7(a) and 4.7(b), the delamination pattern grew in a specific direction and a portion of the PDMS was irreversibly bonded. These results indicate that APTES was not uniformly coated on the surface of the 3D-printed part, and the bonding strength could be improved by optimizing the APTES coating process. The sputter-coated SiO_2 intermediate layer displays a drastically improved bonding strength. We could not determine the definite burst pressure for the sputter-coated SiO_2 layer structure, because the failure occurred at the inlet where the Tygon tubing was epoxy-glued. Therefore, the burst pressure of the test structure with the sputter-coated SiO_2 intermediate layer must be greater than the average burst pressure of 436.65 kPa shown here. As seen in Figure 4.7(a), no delamination was found around the port during that burst test. The bonding was determined to be irreversible, and the results of its peel-off test are shown in Figure 4.7(b).
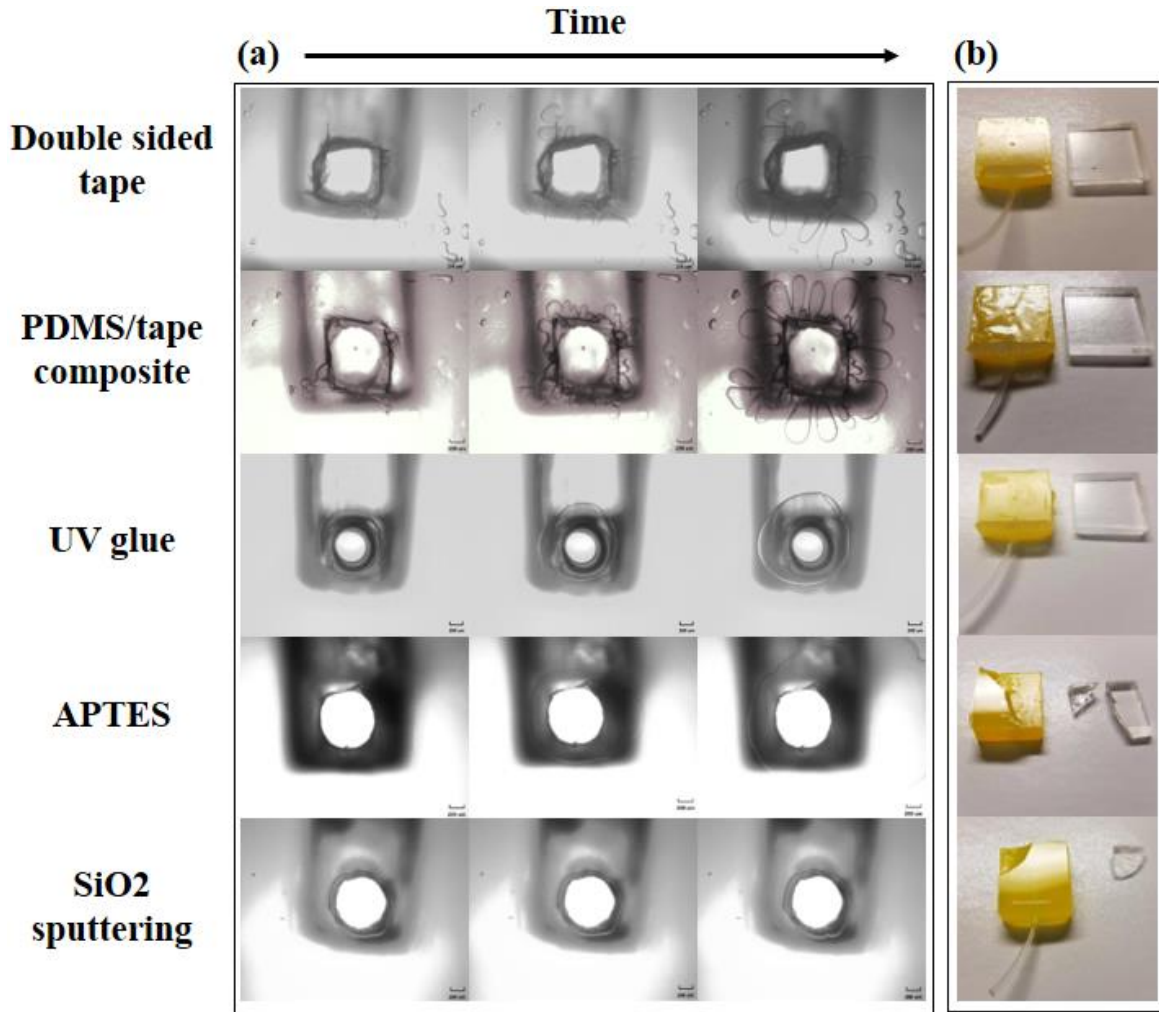
Figure 4.7. (a) Delamination pattern change over time (Note: different time scale for each intermediate layer). (b) The peel-off test results.

The burst test results show that a strong bond between PDMS and the DLP 3D-printed part is achieved with a sputter-coated SiO_2 intermediate layer. The burst pressure greater than 436.65 kPa is comparable to that of other conventional materials used with PDMS for microfluidic devices. The typical burst pressures of PDMS bonded on PDMS and glass using oxygen plasma are 400 kPa and 510 kPa, respectively [131].

To compare the bonding strengths of PDMS to the 3D-printed parts with different resins compared to the yellow resin, we performed the same burst test with emerald and

black resins. The top PDMS parts were fabricated with the same process. The sputter-coated SiO_2 was used as an intermediate layer for both cases and their respective burst pressures were compared with the yellow resin. The results are shown in Figure 4.8(a). Unlike the yellow resin, the burst pressure for the emerald and black resins were 372.32 kPa and 255.11 kPa, respectively. Even though these burst pressures are still higher than that of other intermediate layers, the bonding strengths of PDMS on the 3D-printed parts with emerald and black resins using a sputter-coated SiO_2 intermediate layer is smaller than the yellow resin. Figure 4.8(b) shows the results of the peel-off test. While the PDMS was irreversibly bonded for the emerald resin, only part of the PDMS with the black resin was irreversibly bonded. These results demonstrate that the process used for the yellow resin may not be suitable for other types of resins. The thickness of the SiO_2 layer and the oxygen treatment process must be optimized for each.
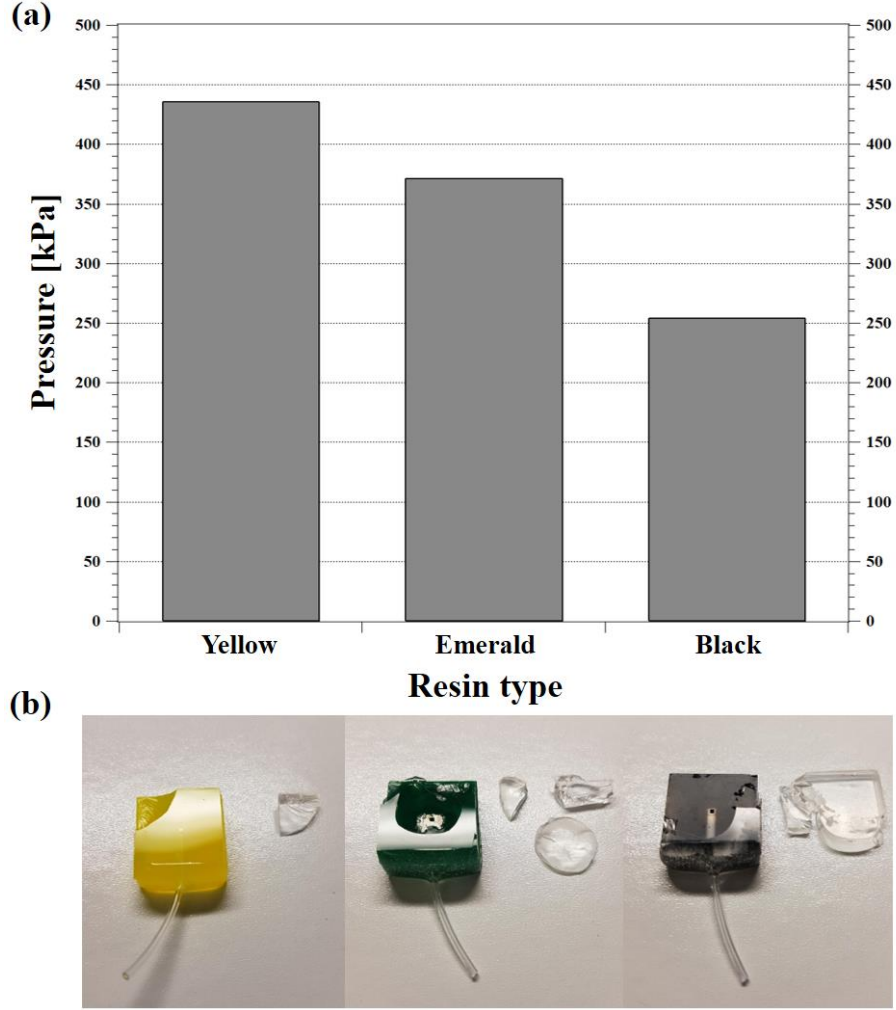
Figure 4.8. (a) Comparison of burst pressure of different types of resins (Yellow, Emerald, Black) using a sputter coated SiO2 layer. (b) The peel off test results.

Using the SiO_2 intermediate layer-based bonding, the microfluidic microinjection device for *Cx. pipiens* embryos without a needle was fabricated. The detailed fabrication processes are shown in Figure 4.9. The mold master for the PDMS top part is 3D-printed using the same DLP 3D printer. The mold master has an inner dimension of 26 mm (width) x 21 mm (length) x 4 mm (height). As shown in Figure 4.9 (a), the degassed PDMS was poured on the TMCS treated mold master (Steps 1-2) and cured in an oven at 65°C for 2 hours. After curing, the PDMS piece was cut along the edge of the mold and

gently peeled off from the mold master (Step 3). Then, the PDMS mold was precisely cut

closer to the needle alignment structure using a razor blade.
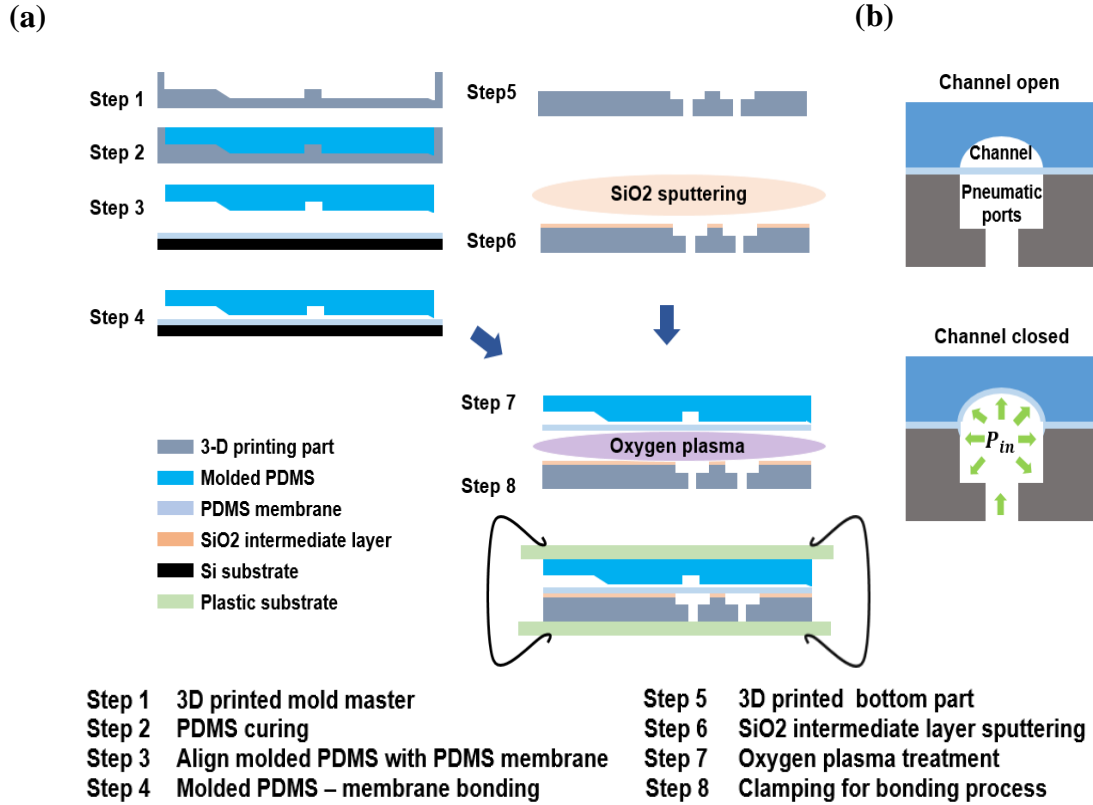
Figure 4.9. (a) Fabrication process of a microfluidic device. (b) The schematic of cross section of a normally open microfluidic valve and its operation.

A normally open microvalve was used to control the fluid flow as shown in

Figure 4.9 (b). For the operation of the microvalve, a thin PDMS membrane is sitting on

top of a pneumatic pressure port. Normally, the valve is open, however, as the pneumatic

pressure is applied, the membrane is deformed and closes the channel. To fabricate a thin

PDMS membrane, the degassed PDMS was spin-coated on TMCS treated 3-inch silicon

substrate. The membrane thickness was controlled by the spin speed. We could achieve a

membrane thickness of 20 μm at 3150 rpm for 1 min. Subsequently, the PDMS coated Si

substrate was partially baked on the hot plate at 55 °C for 10 min. The PDMS piece from

step 3 was gently placed on the partially cured PDMS membrane and was hard baked for

bonding at 100°C for 10 min (Step 4) [121]. Then, the top PDMS part was cut along the

edge and gently peeled off from the Si substrate.

The bottom part of the device is also 3D-printed with the DLP 3D printer using

yellow resin (Step 5). To bond the top PDMS part with the bottom 3D-printed part, a thin

layer of SiO_2 (77 nm) is sputter-coated on the 3D-printed part (Step 6). Both PDMS and

3D-printed part surfaces to be bonded are exposed with oxygen plasma and clamped

together for a strong and uniform bonding (Steps 7 and 8). Figure 4.10(a) shows the

fabricated device. Then, as shown in Figure 4.10(b), Tygon tubing (inner diameter (ID):

0.04") is connected to the inlet and the outlet by gluing with an epoxy. The part where a

capillary needle will be aligned and inserted is covered with double-sided tape and also

glued with an epoxy. Finally, the Tygon tubing is attached to the pneumatic ports with an

epoxy and filled with DI water by applying pressure at 55 kPa for 1 hour. Because PDMS

is gas permeable, air bubbles must be removed for effective valve operation and to

minimize experimental error (Figure 4.11).
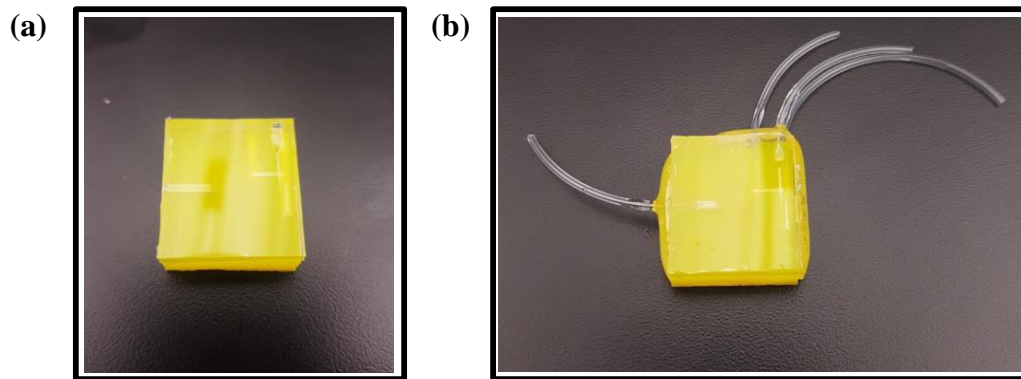
Figure 4.10. (a) Fabricated a microfluidic device (b) Tubing connected a simplified microinjection device.
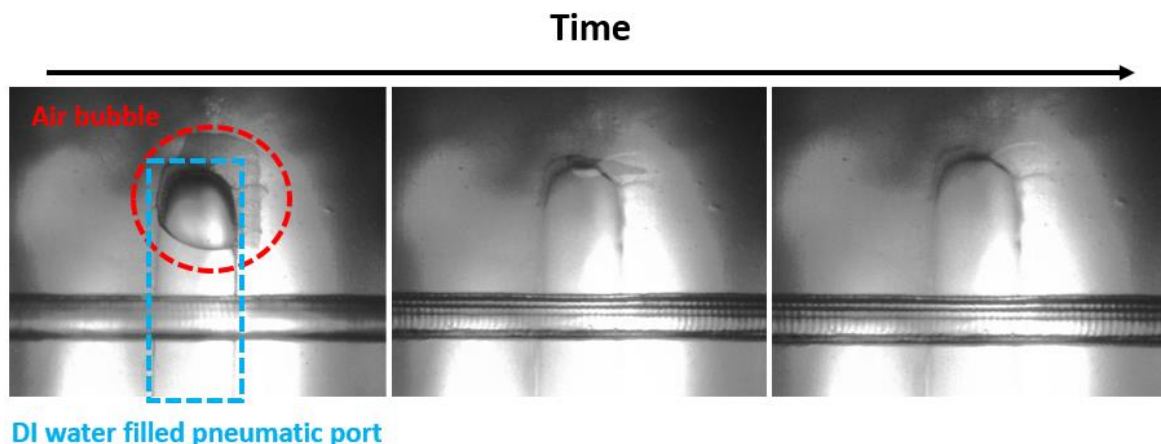
Figure 4.11. Removing air bubble from a pneumatic valve by applying pressure.

The microfluidic control system setup for the microfluidic microinjection device is shown in Figure 4.12. A 2 mL glass syringe is mounted on an infusion/withdraw syringe pumps (EW-74905-04, Cole-Parmer, USA) and connected to the microfluidic device through Tygon tubing (ID: 0.04") and a metal pin. For the valve control, two solenoid valves (MHA1-M1LH-3/2G-0.6-PI, Wolf-Solution, USA) connected in a solenoid valve manifold (CECC-D, Wolf-Solution, USA) are controlled by a solenoid valve controller (CECC-D, Wolf-Solution, USA). The solenoid valve controller is powered by a 24 V power supply. Figure 4.13 illustrates the schematic of the valve control part showing the details. A regulator controls the pressure from the compressed air to the solenoid valve. Two compact regulators (0-450 kPa, McMASTER, USA) were used to limit the pressure applied to pneumatic ports. Polyurethane tubing (PU-156F-0, Cole-Parmer, USA) from the compact regulator was attached to a barbed tube (51525K272, McMASTER, USA). The barbed tube, was then connected to Tygon tubing (inner diameter: 0.04", Cole-Parmer, USA) using a disposable needle tip (22 gauge,

McMASTER, USA). Finally, the Tygon tubing was connected to the microfluidic device

through a metal pin (22RW, New England Small Tube, USA).
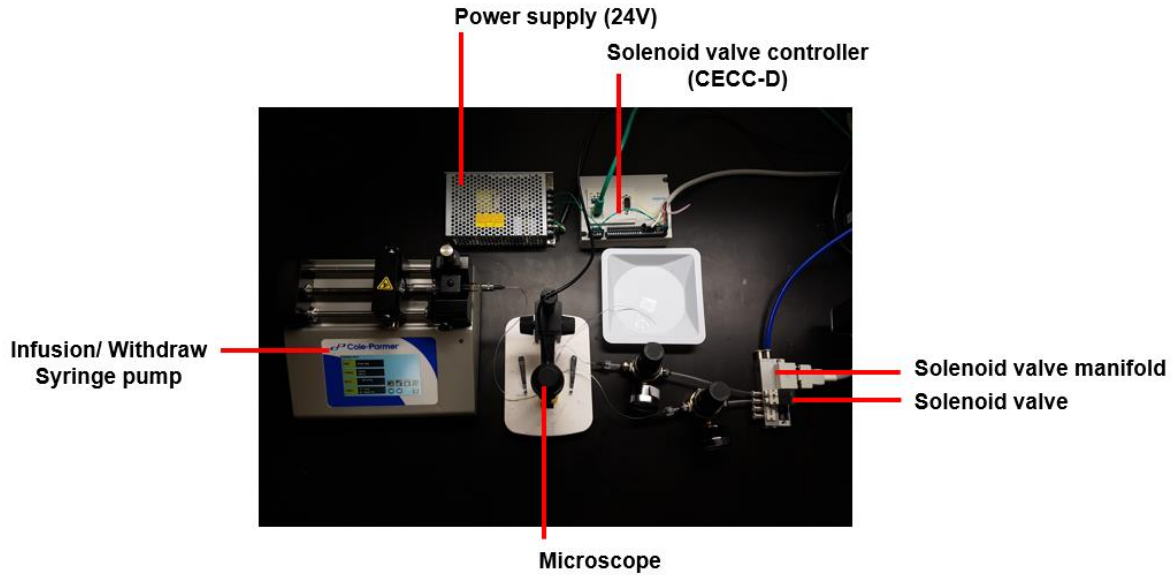
Figure 4.12. Actual image of microfluidic control test setup.
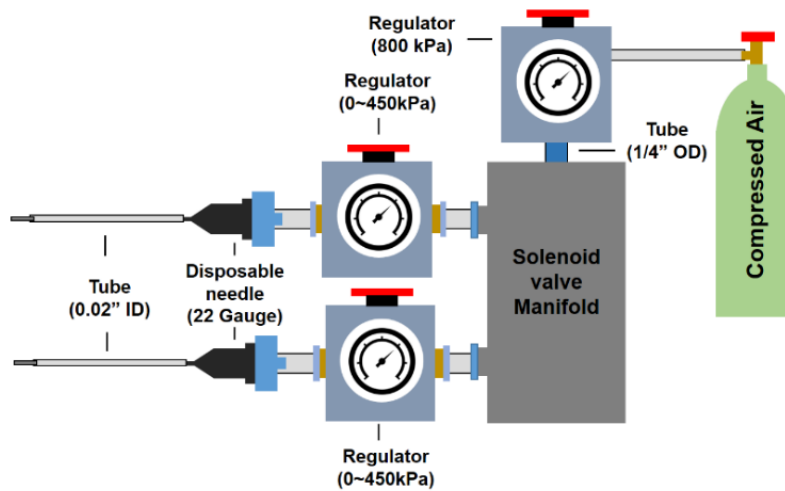
Figure 4.13. The schematic of pneumatic pressure system consisted of the valve control system.

Operation of solenoid valves (ON/OFF) are controlled by applied electrical signals through the controller (CECC-D). The CECC-D controller is a digital input/output (I/O) module, a technique for transferring data between the processor (e.g. computer) and I/O device (e.g. solenoid valve). The input/output of a signal is controlled through software (CODESYS, FESTO, USA). CODESYS is a development environment for programing the controller (CECC-D). The Ladder Logic Diagram is used for the customized programming of the CECC-D. It is a simple and effective language for programming for this type of system. The ladder logic consists of networks and logic elements (Figure 4.14). Each solenoid valve is controlled by networks with logic elements (e.g. contact, coil, etc.). The logic elements operation flows from left to right until it is completed.

In order to control two different solenoid valves, the program designed with logic elements: contacts (input signals) and coils (output) as shown in Figure 4.14(a). This connection can be understood to be similar to a switch (contact, or input signal) and a lamp bulb (coil, or output indicator). First, we inserted contacts to activate the program. Then, we assigned each contact (input) an address number associated with each coil (output), located in the controller. After this, the coils were inserted. Furthermore, to improve user-friendly operation, we employed a visualization toolbox: two switches (contacts) and lamps (coils) to help picture the input/output of signals for solenoid valve operation in CODESYS (Figure 4.14 (a)).

(a)

(b)
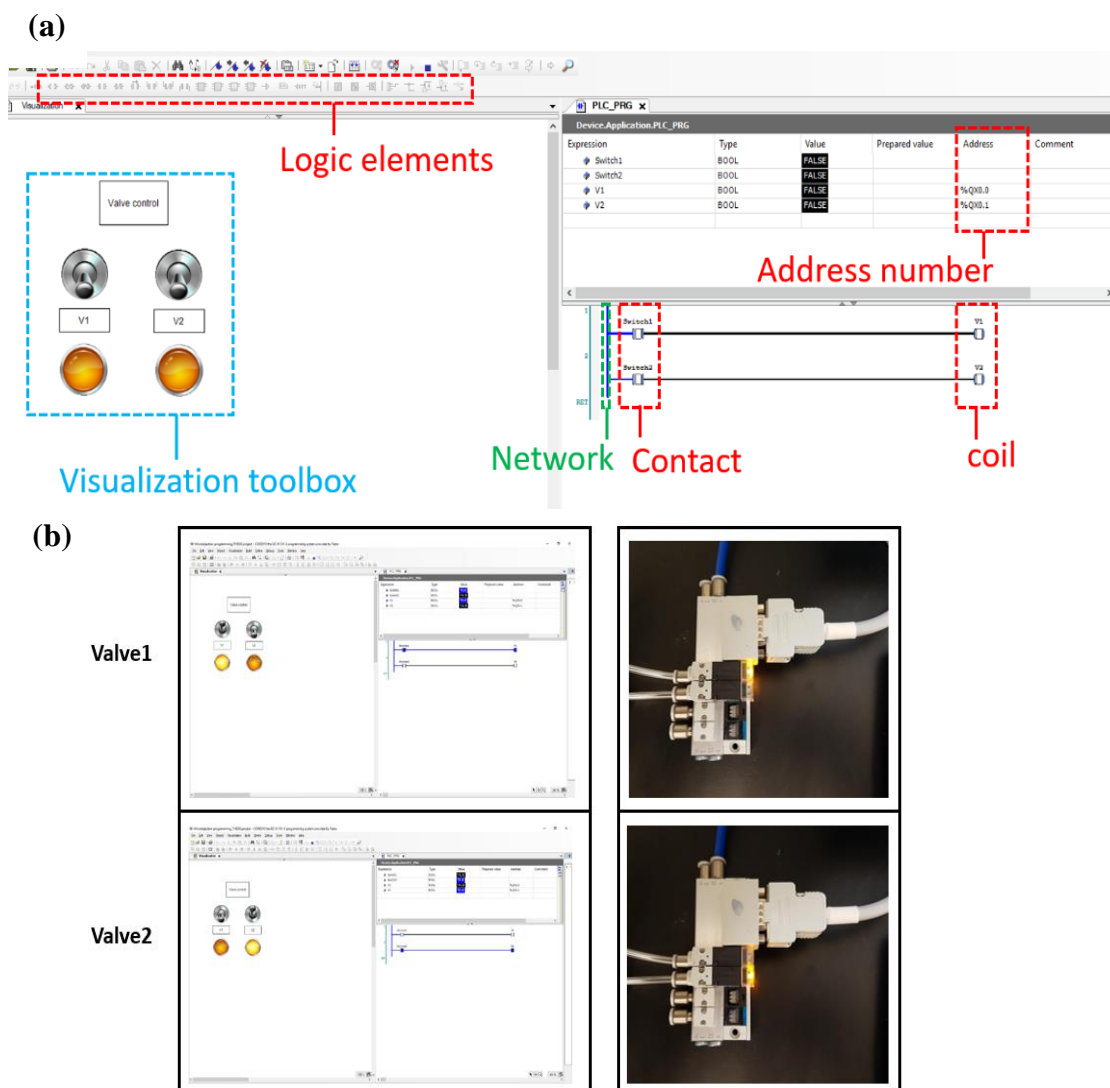
Figure 4.14. (a) Ladder Logic Diagram for programming in CODEYS software. (b) Actual valve control image.

Two different optical microscopes were used to observe the microfluidic device during the operations: a large field digital microscope and a high magnification microscope. To demonstrate the fluid flow control with valves, a low magnification and large field of view digital microscope (USB digital microscope, MUSTECH, China) was used. A high magnification microscope (Olympus BX51, Olympus, USA) was used to observe detailed valve operations and embryo movements in the microchannel.

The fluid control capability of the microfluidic device was demonstrated with red and blue dye solutions. First, we introduced a blue dye into the device using a syringe pump (rate: 10 μL/min). At this stage, V1 in Figure 4.15 was closed with a pressure of 140 kPa, while V2 in Figure 4.15 was open. Figure 4.16 shows the details of V1 and V2 during the valve operation by deforming the PDMS membrane through pneumatic ports as explained in Figure 4.9(b). When there is no pressure applied to the pneumatic ports (images on the left side of Figure 4.16(a) and (b)), the microchannel is open and clearly visible. Upon the pressure applied to the ports, the PDMS membrane is expanded and closes the microchannel blocking the fluid flow along the channel (images on the right side of Figure 4.16 (a) and (b)). The channel filled with a blue dye is shown in Figure 4.15(a). Then, a red dye was introduced into the channel while the V1 was open and V2 was closed with a pressure of 170 kPa as shown in Figure 4.15(b). Immediately after releasing V1 and closing V2, the left side of channel is filled with the blue dye solution due to the pressure existing along the fluid path. Then, the Tygon tubing is filled with red dye and reconnected to the device. As the red dye was pumped into the device with a flow rate of 10 μL/min, air passed through and emptied the channel before the red dye filled the channel. The results clearly indicate the valves work properly to control the fluid flow inside the microfluidic device.
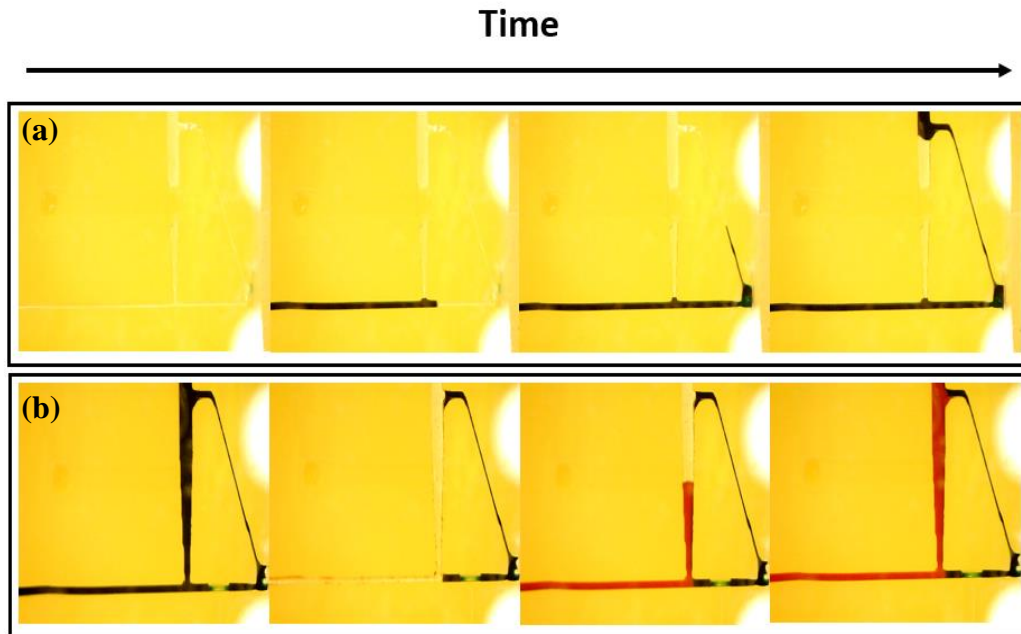
Figure 4.15. Microscope image of fluid test using dye solution (a) Introducing blue dye solution (V1: closed, V2: open). (b) Introducing red dye solution (V1: open, V2: closed).
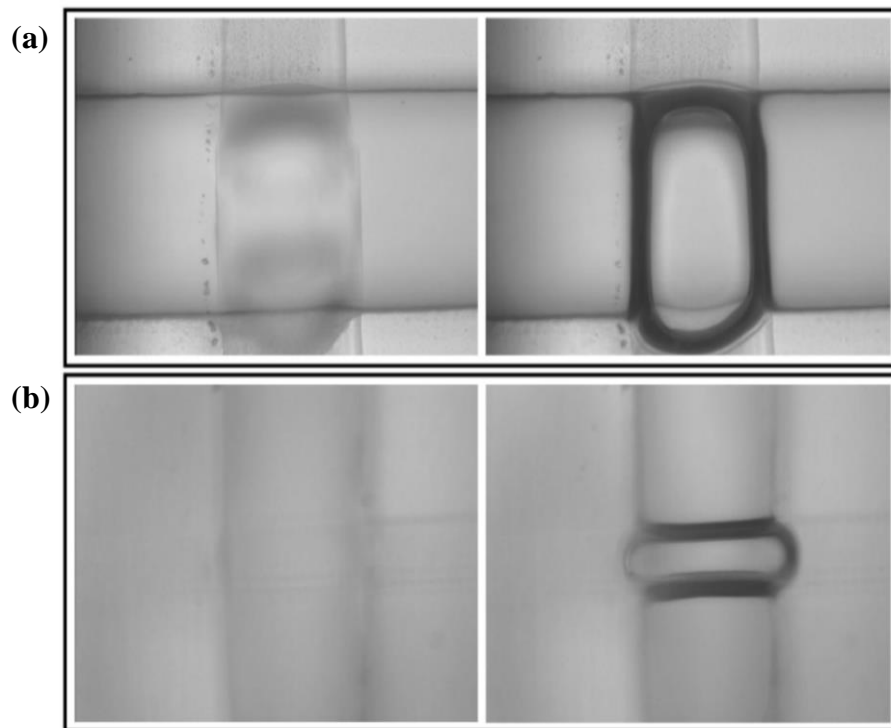
Figure 4.16. Microscope image of valve operation from the top view (a) V1 (left: open state, right: closed state) (b) V2 (left: open state, right: closed state).

To observe the behavior of the *Cx. pipiens* embryo in the microfluidic channel and the embryo handling capability of the microfluidic channel, a single embryo was collected and loaded into the microfluidic device. As shown in Figure 4.17(b), mosquitoes lay dozens of embryos connected together to form a raft that float on the water surface. Since the embryo injection process is performed one by one, the embryos need to be separated before loading into the device. Rafts of embryos were place on a wet paper with a white mineral oil (Klearol oil, Sonneborn, USA), harmless to the embryos, in a weighing boat as shown in Figure 4.17(b). A thin brush is used to separate embryos from the rafts (Figure 4.17(c)). Then, the mineral oil was poured into the boat and let embryos float (Figure 4.17(d)).
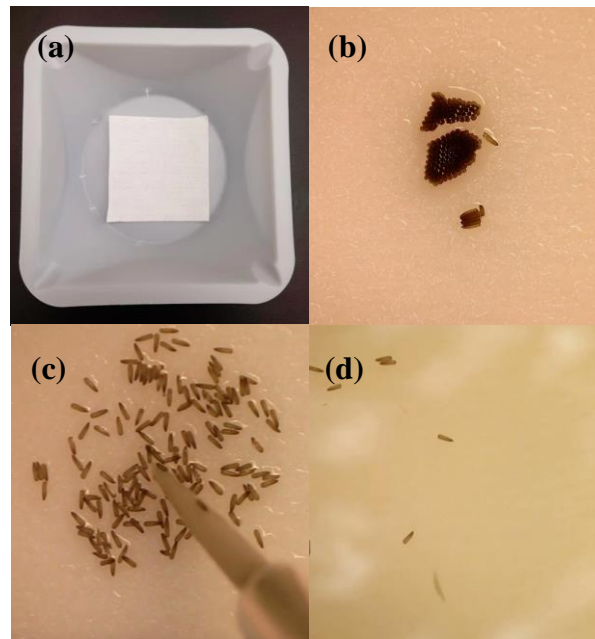
Figure 4.17. (a) Weighting boat for embryo separation process. (b) Putting *Cx. pipiens* embryos on the weighting boat. (c) Embryo separation process using thin brush. (d) Pouring white mineral oil in weighting boat.

A Tygon tubing with a syringe is used to load embryos into it. V1 was closed andV2 was open while an embryo is loaded into the microfluidic channel with the syringe pump at a flow rate of 100 µL/min. The embryo in the microfluidic device is shown in Figure 4.18. The images at the top show the embryo passing through the T-junction in the device (Figure 4.18(a)). As the embryo was continuously pushed, it reached the injection location where the embryo sticks to the guide structure. This will be the injection site once a capillary needle is integrated in the device (Figure 4.18(b)). The embryo is then unloaded along the T-junction as shown in the Figure 4.18(c). This experiment clearly shows the microfluidic device works as expected with the controllers and this device can be used for the successful microinjection of *Cx. pipien*s embryos if we integrate a capillary needle with it.

Figure 4.18. Image of embryo control test (a) Embryo loading at T-junction. (b) Embryo loading at guide structure. (c) Embryo unloading at T-junction.

CHAPTER FIVE

Conclusion and Future Work

Conclusion

Mosquito-borne diseases, such as Malaria, Dengue, Zika and West Nile Virus, cause millions of deaths each year and the impact of mosquito-borne diseases is rapidly growing. To address epidemics of these fatal infectious diseases, there have been active research efforts on vector control through genetically modifying mosquitoes. The altered mosquitoes are produced through transfection, which is the process of introducing genetic biomolecules (e.g. proteins, nucleic acids, and antibodies) into embryos. While various biological, chemical, and physical transfection methods have been developed, the gold standard of mosquito embryo transfection is still a manual capillary microinjection method. The manual capillary microinjection method is a very labor-intensive method with a low throughput and a high operator skill dependence, which hinders the research progress for mosquito embryo transfection-based vector control to reduce mosquito-borne diseases. A microfluidic-based microinjection device that integrates a capillary needle with a microfluidic device has been proposed to improve the throughput and success rate of the transfection, regardless of the operators' skill level.

In this thesis, the details of the proposed microfluidic-based microinjection device were discussed, the fabrication processes using PDMS and 3D printing were successfully developed, and fluid control and embryo manipulation capabilities of the microfluidic device without a capillary needle were experimentally demonstrated.

The target microchannel dimension (height: 200 µm, width: 200 µm) was achieved when we set the design parameter for a 300 µm height and a 150 µm width. Furthermore, symmetrical microchannels could be printed by adding error correction structures, designed with a height of 180 µm and a width of 60 µm. The target angle of the guide structure, corresponding to the angle of embryo posterior pole (27°), was achieved by designing the taper with an angle of 30 °.

The sputter-coated SiO_2 intermediate layer with a thickness of 77 nm demonstrated the highest bonding strength compared to other intermediate layers: double-sided tape, a PDMS/tape composite, UV glue, (3-Aminopropyl) triethoxysilane (APTES). The burst pressure with this SiO_2 intermediate layer was greater than 436.65 kPa. Furthermore, we measured the burst pressure using the same SiO_2 intermediate layer process for two other resins (emerald and black). The burst pressures for these were less than that of the yellow resin. The results indicate that the intermediate layer thickness and oxygen treatment processes have to be optimized for each resin.

The microfluidic device was successfully designed using determined design parameters. It was fabricated through 3D printing, PDMS casting, and bonding using the sputter-coated SiO_2 intermediate layer. We conducted a fluidic control experiment using dye solutions (red and blue) using a fabricated device sample. The introduced dye solutions with flow rate of 10 µL/min were controlled by two valves. Two valves operated at different applied pressures (V1: 140 kPa, V2: 170 kPa) by deforming the PDMS membrane through pneumatic ports. Furthermore, the microfluidic device successfully loaded an embryo, moved the embryo to the injection location through a T junction, and unloaded the embryo. This experiment clearly demonstrates the

66

microfluidic device works as expected with the controllers. Moreover, this device can be used for the microinjection of *Cx. pipiens* embryos if we combine a capillary needle with it.
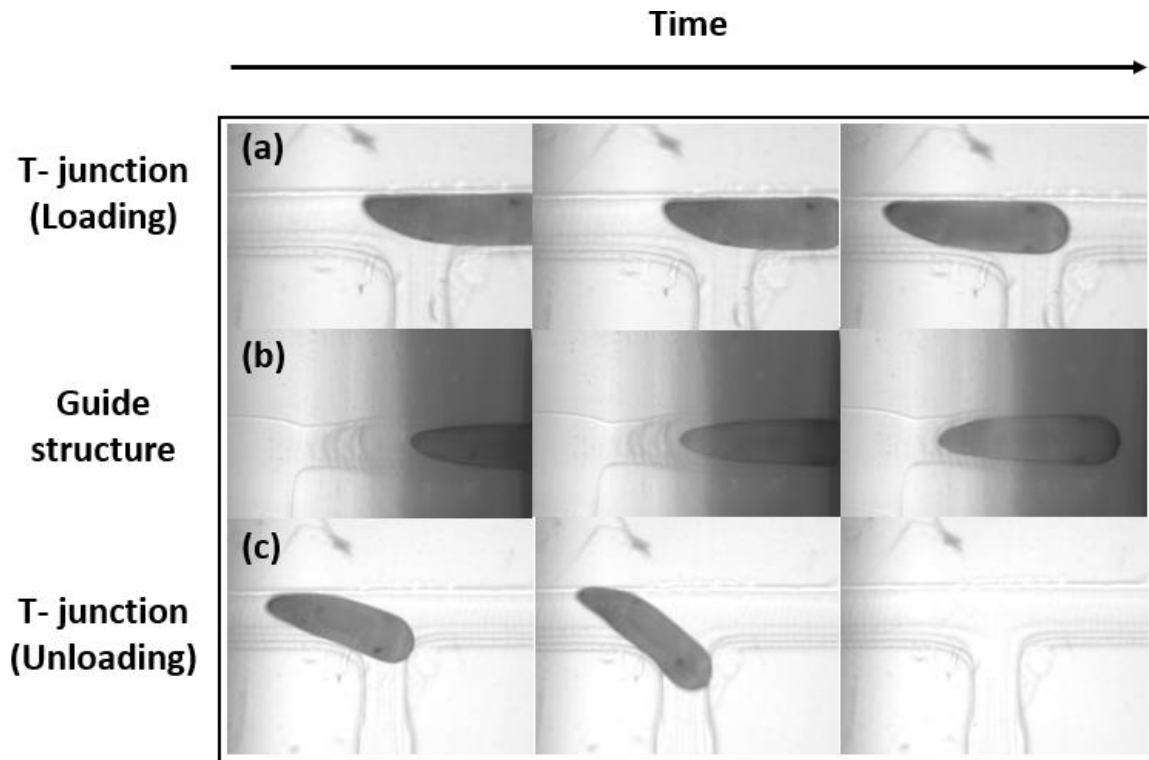
Future Work

Overall our microfluidic device and its controller were successfully fabricated without a capillary injection needle. However, further study is necessary to successfully achieve a microinjection using the proposed microfluidic device, with the addition of a capillary injection needle.

Needle Alignment and Integration

In order for successful transfection, precise needle alignment and sturdy integration into the rest of microfluidic device are important. A glass needle tip must be short (~150 μm), accurately positioned, and perfectly fixed to prevent the movement of the needle tip during the injection process. Needle alignment structures are suggested to accurately position the needle. Without it, it will be very difficult to consistently place needles, even with an accurate XYZ-micropositioner. The alignment structure must be designed so that accurate alignment and positioning of the needle can be achieved quickly. A method of fixing the needle for a sturdy integration with the rest of microfluidic device must be developed to avoid any leakage through the needle. The opening for the needle must be as small as possible, and bonding material as simple as a thick glue could be used to fix the needle without blocking the channel through the small opening.

Reagent Volume Control

A pneumatic control system to control the reagent volume injected into the embryo should also be developed. A solenoid valve can be used with the pneumatic control system as discussed in the Chapter 4. The volume of reagent delivered will be controlled by the injection pressure and the duration of the automated pressure pulse. The pressure and the pulse duration have to be optimized in order to deliver the exact volume of reagent.

Dual Needle System

Since the injection has to be performed at the posterior pole of embryos, it may be necessary to implement a dual needle system with two capillary needles. When an embryo is loaded into the microfluidic device, the embryo can have two possible orientations.
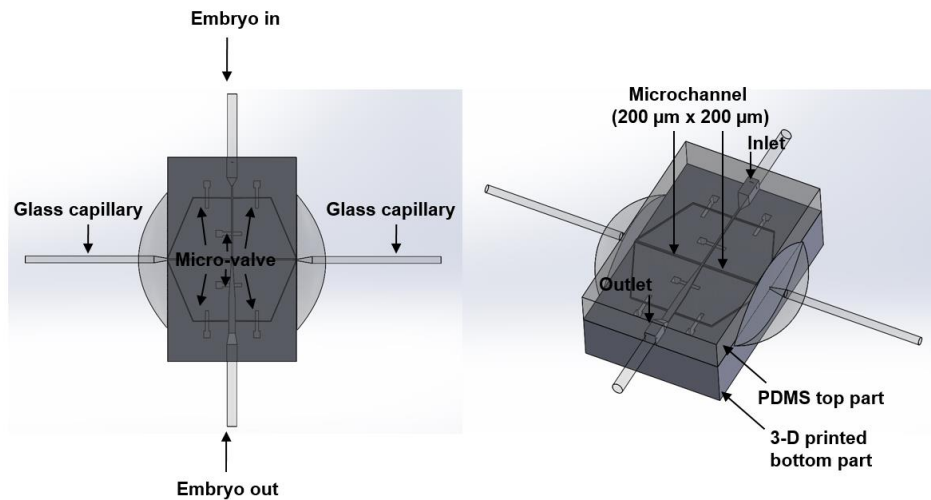
Figure 5.1. Dual Needle system image.

Demonstrate Injection Efficiency and Survival Rate

The injection efficiency and the survival rate of embryos with the microfluidic microinjection device must be determined. Green Fluorescent Protein (GFP) (exciting wavelength: 488 nm, emitting wavelength: 510 nm [132]) could be used for this purpose. The successfully injected embryo will show a green fluorescence signal. In order to find injection efficiency, the number of the embryos with the fluorescence signal will be divided by the total number of injected embryos [133]. The injected embryo will be incubated for 24 hours to study the cell survival rate after the injection process. The survival rate is defined as a ratio of the number of fluorescent embryos after 24 hours of injection to the number of the fluorescent embryos right after injection [133].

REFERENCES

[1] B. Adams and D. D. Kapan, "Man Bites Mosquito: Understanding the Contribution of Human Movement to Vector-Borne Disease Dynamics," *PLOS ONE*, vol. 4, no. 8, p. e6763, Aug. 2009.

[2] E. Barclay, "Is climate change affecting dengue in the Americas?," *The Lancet*, vol. 371, no. 9617, pp. 973–974, Mar. 2008.

[3] D. J. Gubler, "Dengue, Urbanization and Globalization: The Unholy Trinity of the 21st Century," *Trop.Med.Health*, vol. 39, no. 4SUPPLEMENT, pp. S3–S11, 2011.

[4] "Microcephaly," *World Health Organization*. [Online]. Available: http://www.who.int/news-room/fact-sheets/detail/microcephaly. [Accessed: 16-Sep-2018].

[5] M. R. Duffy, T.-H. Chen, W. T. Hancock, A. M. Powers, J. L. Kool, R. S. Lanciotti , M. Pretrick, M. Marfel, S. Holzbauer, C. Dubray, L. Guilaumot, A. Griggs."Zika Virus Outbreak on Yap Island, Federated States of Micronesia," *New England Journal of Medicine*, vol. 360, no. 24, pp. 2536–2543, Jun. 2009.

[6] CDC, "Reporting and Surveillance - Zika Virus," *Centers for Disease Control and Prevention*, 12-Jan-2017. [Online]. Available: http://www.cdc.gov/zika/reporting/index.html. [Accessed: 16-Sep-2018].

[7] V.-M. Cao-Lormeau, C. Roche, A. Teissier, E. Robin, A.-L. Berry, H.-P. Mallet, A. A. Sall, D. Musso, "Zika Virus, French Polynesia, South Pacific, 2013," *Emerg Infect Dis*, vol. 20, no. 6, pp. 1085–1086, Jun. 2014.

[8] S. Beare, E. Simpson, K. Gray, and D. Andjelic, "Rapid Integration of Zika Virus Prevention Within Sexual and Reproductive Health Services and Beyond: Programmatic Lessons From Latin America and the Caribbean," *Global Health: Science and Practice*, vol. 7, no. 1, pp. 116–127, Mar. 2019.

[9] "WHO | 6 November 2015, vol. 90, 45 (pp. 609–616)," *WHO*. [Online]. Available: http://www.who.int/wer/2015/wer9045/en/. [Accessed: 26-May-2019].

[10] M. Hennessey, M. Fischer, and J. E. Staples, "Zika Virus Spreads to New Areas — Region of the Americas, May 2015–January 2016," *American Journal of Transplantation*, vol. 16, no. 3, pp. 1031–1034, 2016.

[11] L. Schuler-Faccini, E. M. Ribeiro, I. M. L. Feitosa, D. D. G. Horovitz, D. P. Cavalcanti, A. Pessoa, M. J. R. Doriqui, J. I. Neri, J. M. de P. Neto, H. Y. C. Wanderley, M. Cernach, A. S. El-Husny, M. V.S. Pone, C. I. C. Serao, M. T. V. Samseverino, "Possible Association Between Zika Virus Infection and Microcephaly - Brazil, 2015," *MMWR Morb. Mortal. Wkly. Rep.*, vol. 65, no. 3, pp. 59–62, Jan. 2016.

[12] C. G. Victora, L. Schuler-Faccini, A. Matijasevich, E. Ribeiro, A. Pessoa, and F. C. Barros, "Microcephaly in Brazil: how to interpret reported numbers?," *The Lancet*, vol. 387, no. 10019, pp. 621–624, Feb. 2016.

[13] "WHO | WHO Report on Global Surveillance of Epidemic-prone Infectious Diseases - Yellow fever," *WHO*. [Online]. Available: http://www.who.int/csr/resources/publications/yellowfev/CSR_ISR_2000_1/en/index3.html. [Accessed: 20-Jul-2018].

[14] B.-H. Song, S.-I. Yun, M. Woolley, and Y.-M. Lee, "Zika virus: History, epidemiology, transmission, and clinical presentation," *Journal of Neuroimmunology*, vol. 308, pp. 50–64, Jul. 2017.

[15] "Dengue and severe dengue," *World Health Organization*. [Online]. Available: http://www.who.int/news-room/fact-sheets/detail/dengue-and-severe-dengue. [Accessed: 20-Jul-2018].

[16] S. B. Halstead, "Dengue vaccine development: a 75% solution?," *The Lancet*, vol. 380, no. 9853, pp. 1535–1536, Nov. 2012.

[17] S. Bhatt, P. W. Gething, O. J. Brady,J. P. Messina, A. W. Farlow, C. L. Moyes, J. M. Drake, J. S. Brownstein, A. G. Hoen, O. Sankoh, M. F. Myers, D. B. George, T. Jaenisch, G. R. W. Wint, C. P. Simmons, T. W. Scott, J. J. Farrar, S. I. Hay, "The global distribution and burden of dengue," *Nature*, vol. 496, no. 7446, pp. 504–507, Apr. 2013.

[18] "Epidemiology | Dengue | CDC." [Online]. Available: https://www.cdc.gov/dengue/epidemiology/index.html. [Accessed: 20-Jul-2018].

[19] "WHO | Epidemiology," *WHO*. [Online]. Available: http://www.who.int/denguecontrol/epidemiology/en/. [Accessed: 20-Jul-2018].

[20] "Yellow fever," *World Health Organization*. [Online]. Available: http://www.who.int/news-room/fact-sheets/detail/yellow-fever. [Accessed: 20-Jul-2018].

[21] T. P. Monath, J. P. Woodall, D. J. Gubler, T. M. Yuill, J. S. Mackenzie, R. M. Martins, P. Reiter, D. L. Heymann, "Yellow fever vaccine supply: a possible solution," *The Lancet*, vol. 387, no. 10028, pp. 1599–1600, Apr. 2016.

[22] T. P. Monath and P. F. C. Vasconcelos, "Yellow fever," *Journal of Clinical Virology*, vol. 64, pp. 160–173, Mar. 2015.

[23] T. Garske, M.D.V. Kerkhove, S. Yactayo, O. Ronveaux, R.F. Lewis, J. E. Staples,W. Perea, N. M. Ferguson, "Yellow Fever in Africa: Estimating the Burden of Disease and Impact of Mass Vaccination from Outbreak and Serological Data," *PLOS Medicine*, vol. 11, no. 5, p. e1001638, May 2014.

[24] "Yellow fever situation report." World Health Organization, 28-Oct-2016.

[25] "WHO | Yellow fever – Brazil," *WHO*. [Online]. Available: http://www.who.int/csr/don/09-march-2018-yellow-fever-brazil/en/. [Accessed: 26-May-2019].

[26] C. Caglioti, E. Lalle, C. Castilletti, F. Carletti, M. R. Capobianchi, and L. Bordi, "Chikungunya virus infection: an overview," p. 18.

[27] "Chikungunya," *World Health Organization*. [Online]. Available: http://www.who.int/news-room/fact-sheets/detail/chikungunya. [Accessed: 16-Sep-2018].

[28] S. C. Weaver, "Arrival of Chikungunya Virus in the New World: Prospects for Spread and Impact on Public Health," *PLOS Neglected Tropical Diseases*, vol. 8, no. 6, p. e2921, Jun. 2014.

[29] L. Pezzi, C. B. Reusken, S. C. Weaver, J. F. Drexler, M. Busch, A. D. LaBeaud, M. S. Diamond, N. Vasilakis, M. A. Drebot, A. M. Siqueira, G.S. Ribeiro, A. Kohl, M. Lecuit, L.F.P. Ng, P. Gallian, X. de Lamballerie, "GloPID-R report on Chikungunya, O'nyong-nyong and Mayaro virus, part I: Biological diagnostics," *Antiviral Research*, vol. 166, pp. 66–81, Jun. 2019.

[30] "Number of Reported Cases of Chikungunya Fever in the Americas, by Country or Territory 2014." Pan American Health Organization.

[31] "Number of Reported Cases of Chikungunya Fever in the Americas, by Country or Territory 2015." Pan American Health Organization.

[32] "Number of Reported Cases of Chikungunya Fever in the Americas, by Country or Territory 2016." Pan American Health Organization.

[33] "Number of Reported Cases of Chikungunya Fever in the Americas, by Country or Territory 2017." Pan American Health Organization.

[34] "West Nile virus." [Online]. Available: https://www.who.int/news-room/fact-sheets/detail/west-nile-virus. [Accessed: 26-May-2019].

[35] M. Y. Chowers, R. Lang, F. Nassar, D. Ben-David, M. Giladi, E. Rubinshtein, A. Itzhaki, J. Mishal, Y. Siegman-Igra, R. Kitzes, N. Pick, Z. Landau, D. Wolf, H. Bin, E. Mendelson, S. D. Pitlik, M. Weomberger, "Clinical characteristics of the West Nile fever outbreak, Israel, 2000.," *Emerg Infect Dis*, vol. 7, no. 4, pp. 675–678, 2001.

[36] A. Sirbu, C. S. Ceianu, R. I. Panculescu-Gatej, A. Vázquez, A. Tenorio, R. Rebreanu, M. Niedrig, G. Nicolescu, A. Pistol, "Outbreak of West Nile virus infection in humans, Romania, July to October 2010," Jan. 2011.

[37] A. Papa, K. Danis, A. Baka, A. Bakas, G. Dougas, T. Lytras, G. Theocharopoulos, D. Chrysagis, E. Vassiliadou, F. Kamaria, A Liona, K Mellou, G Saroglou, T Panagiotopoulos, "Ongoing outbreak of West Nile virus infections in humans in Greece, July – August 2010," *Eurosurveillance*, vol. 15, no. 34, p. 19644, Aug. 2010.

[38] "Final Cumulative Maps and Data | West Nile Virus | CDC," 10-Dec-2018. [Online]. Available: https://www.cdc.gov/westnile/statsmaps/cumMapsData.html. [Accessed: 26-May-2019].

[39] "Transmission | Dengue | CDC," 06-May-2019. [Online]. Available: https://www.cdc.gov/dengue/transmission/index.html. [Accessed: 25-May-2019].

[40] H. Seda, "Dengue and the Aedes aegypti mosquito." .

[41] "*Aedes aegypti*," *Wikipedia*. 31-Mar-2019.

[42] L. Eisen and C. G. Moore, "Aedes (Stegomyia) aegypti in the Continental United States: A Vector at the Cool Margin of Its Geographic Range," *J Med Entomol*, vol. 50, no. 3, pp. 467–478, May 2013.

[43] "Resources – Toledo Area Sanitary District." .

[44] F. L. Soper, "The Elimination of Urban Yellow Fever in the Americas Through the Eradication of Aedes aegypti," *Am J Public Health Nations Health*, vol. 53, no. 1, pp. 7–16, Jan. 1963.

[45] O. P. Severo, "Eradication of the Aedes Aegypti Mosquito from the Americas," 1955.

[46] E. B. Kauffman and L. D. Kramer, "Zika Virus Mosquito Vectors: Competence, Biology, and Vector Control," *J Infect Dis*, vol. 216, no. suppl_10, pp. S976–S990, Dec. 2017.

[47] C. L. Moyes, J. Vontas, A. J. Martins, L. C. Ng, S. Y. Koou, I. Dusfour, K. Raghavendra, J. Pinto, V. Corbel, J. -P. David, D. Weetman, "Contemporary status of insecticide resistance in the major Aedes vectors of arboviruses infecting humans," *PLOS Neglected Tropical Diseases*, vol. 11, no. 7, p. e0005625, Jul. 2017.

[48] K. Gorman, J. Young, L. Pineda, R. Márquez, N. Sosa, D. Bernal, R. Torres, Y. Soto, R. Lacroix, N. Naish, P. Kaiser, K. Tepedino, G. Philips, C. Kosmann, L. Caceres, "Short-term suppression of Aedes aegypti using genetic control does not facilitate Aedes albopictus," *Pest Management Science*, vol. 72, no. 3, pp. 618–628.

[49] A. F. Harris, A. R. McKemey, D. Nimmo, Z. Curtis, I. Black, S. A. Morgan, M. N. Oviedo, R. Lacroix, N. Naish, N. I. Morrison, A. Collado, J. Stevenson, S. Scaife, T. D. Alla, G. Fu, C. Phillips, A. Miles, N. Raduan, N. Kelly, C. Beech, C. A. Donnelly, W. D. Petrie, L. Alphey, "Successful suppression of a field mosquito population by sustained release of engineered male mosquitoes," *Nature Biotechnology*, 10-Sep-2012. [Online]. Available: https://www.nature.com/articles/nbt.2350. [Accessed: 19-Jul-2018].

[50] D.O. Carvalho, A. R. McKemey, L. Garziera, R. Lacroix, C.A. Donnelly, L. Alphey, A. Malavasi, M. L. Capurro, "Suppression of a Field Population of Aedes aegypti in Brazil by Sustained Release of Transgenic Male Mosquitoes," *PLOS Neglected Tropical Diseases*, vol. 9, no. 7, p. e0003864, Jul. 2015.

[51] F. Recillas-Targa, "Multiple strategies for gene transfer, expression, knockdown, and chromatin influence in mammalian cell lines and transgenic animals," *Mol Biotechnol*, vol. 34, no. 3, pp. 337–354, Nov. 2006.

[52] D. J. Glover, H. J. Lipps, and D. A. Jans, "Towards safe, non-viral therapeutic gene expression in humans," *Nature Reviews Genetics*, vol. 6, no. 4, p. 299, Apr. 2005.

[53] A. Noori, P. Ravi Selvaganapathy, and J. Wilson, "Microinjection in a microfluidic format using flexible and compliant channels and electroosmotic dosage control," *Lab on a Chip*, vol. 9, no. 22, pp. 3202–3211, 2009.

[54] R. Ghaemi, "MICROFLUIDIC DEVICE FOR MICROINJECTION OF CAENORHABDITIS ELEGANS," thesis, 2014.

[55] T. K. Kim and J. H. Eberwine, "Mammalian cell transfection: the present and the future," *Anal Bioanal Chem*, vol. 397, no. 8, pp. 3173–3178, Aug. 2010.

[56] W. Ding, E. Bergeron, R. Lachaine, and M. Meunier, "Nanomaterial-assisted light-induced poration and transfection of mammalian cells," in *Applications of Nanoscience in Photomedicine*, Elsevier, 2015, pp. 331–376.

[57] K. Takahashi and S. Yamanaka, "Induction of Pluripotent Stem Cells from Mouse Embryonic and Adult Fibroblast Cultures by Defined Factors," *Cell*, vol. 126, no. 4, pp. 663–676, Aug. 2006.

[58] E. T. Schenborn and V. Goiffon, "DEAE-Dextran Transfection of Mammalian Cultured Cells," in *Transcription Factor Protocols*, M. J. Tymms, Ed. Totowa, NJ: Humana Press, 2000, pp. 147–153.

[59] "Efficient lipid-mediated transfection of DNA into primary rat hepatocytes | SpringerLink." [Online]. Available: https://link.springer.com/article/10.1007/BF02634283. [Accessed: 16-Sep-2018].

[60] P. Washbourne and A. K. McAllister, "Techniques for gene transfer into neurons," *Current Opinion in Neurobiology*, vol. 12, no. 5, pp. 566–573, Oct. 2002.

[61] "Biolistic transfection of neuronal cultures using a hand-held gene gun | Nature Protocols." [Online]. Available: https://www.nature.com/articles/nprot.2006.145. [Accessed: 13-Sep-2018].

[62] D. C. Lo, A. K. McAllister, and L. C. Katz, "Neuronal transfection in brain slices using particle-mediated gene transfer," *Neuron*, vol. 13, no. 6, pp. 1263–1268, Dec. 1994.

[63] J. Gehl, "Electroporation: theory and methods, perspectives for drug delivery, gene therapy and research," *Acta Physiologica Scandinavica*, vol. 177, no. 4, pp. 437–447, Apr. 2003.

[64] T. Inoue and R. Krumlauf, "An impulse to the brain--using in vivo electroporation," *Nature Neuroscience*, 01-Nov-2001. [Online]. Available: http://link.galegroup.com/apps/doc/A185565542/AONE?sid=googlescholar. [Accessed: 13-Sep-2018].

[65] D. Ino and M. Iino, "In Vivo Gene Transfer to Schwann Cells in the Rodent Sciatic Nerve by Electroporation," *JoVE (Journal of Visualized Experiments)*, no. 115, p. e54567, Sep. 2016.

[66] H. Shi, L. Ruan, I. Söderhäll, K. Söderhäll, and X. Xu, "Transfection of crayfish hematopoietic tissue cells," *Developmental & Comparative Immunology*, vol. 88, pp. 70–76, Nov. 2018.

[67] D. Zhao, D. Huang, Y. Li, M. Wu, W. Zhong, Q. Cheng, X. Wang, Y. Wu, X. Zhou, Z. Wei, Z. Li, Z. Liang, "A Flow-Through Cell Electroporation Device for Rapidly and Efficiently Transfecting Massive Amounts of Cells *in vitro* and *ex vivo*," *Scientific Reports*, vol. 6, p. 18469, Jan. 2016.

[68] H. J. Kim, J. F. Greenleaf, R. R. Kinnick, J. T. Bronk, and M. E. Bolander, "Ultrasound-Mediated Transfection of Mammalian Cells," *Human Gene Therapy*, vol. 7, no. 11, pp. 1339–1346, Jul. 1996.

[69] Y. Liu, H. Yang, and A. Sakanishi, "Ultrasound: Mechanical gene transfer into plant cells by sonoporation," *Biotechnology Advances*, vol. 24, no. 1, pp. 1–16, Jan. 2006.

[70] S. Le Gac, E. Zwaan, A. van den Berg, and C.-D. Ohl, "Sonoporation of suspension cells with a single cavitation bubble in a microfluidic confinement," *Lab on a Chip*, vol. 7, no. 12, pp. 1666–1672, 2007.

[71] R. Abdalkader, S. Kawakami, J. Unga, Y. Higuchi, R. Suzuki, K. Maruyama, F. Yamashita, M. Hashida, "The development of mechanically formed stable nanobubbles intended for sonoporation-mediated gene transfection," *Drug Delivery*, vol. 24, no. 1, pp. 320–327, Jan. 2017.

[72] A. Tsuchiya, J.-H. Kang, T. Mori, Y. Naritomi, S. Kushio, T. Niidome, K. Tachibana, Y. Takahashi, Y. Negishi, Y. Oda, R. Suzuki, K. Maruyama, Y. Katayama, "Efficient delivery of signal-responsive gene carriers for disease-specific gene expression via bubble liposomes and sonoporation," *Colloids and Surfaces B: Biointerfaces*, vol. 160, pp. 60–64, Dec. 2017.

[73] C. Yao, Z. Zhang, R. Rahmanzadeh, and G. Huettmann, "Laser-Based Gene Transfection and Gene Therapy," *IEEE Transactions on NanoBioscience*, vol. 7, no. 2, pp. 111–119, Jun. 2008.

[74] "New Technique for Gene Transfection Using Laser Irradiation | Journal of Investigative Medicine." [Online]. Available: https://jim.bmj.com/content/49/2/184?utm_source=trendmd&utm_medium=cpc&ut m_campaign=jim&utm_content=consumer&utm_term=0-A. [Accessed: 13-Sep-2018].

[75] L. Thobakgale, S. Manoto, S. O. Lemboumba, M. Maaza, and P. Mthunzi-Kufa, "Femtosecond laser assisted photo-transfection and differentiation of mouse embryonic stem cells," in *Optical Interactions with Tissue and Cells XXIX*, 2018, vol. 10492, p. 1049205.

[76] O. Guillaume-Gentil, E. Potthoff, D. Ossola, P. Dörig, T. Zambelli, and J. A. Vorholt, "Force-Controlled Fluidic Injection into Single Cell Nuclei," *Small*, vol. 9, no. 11, pp. 1904–1907, Jun. 2013.

[77] W. Wang, X. Liu, D. Gelinas, B. Ciruna, and Y. Sun, "A Fully Automated Robotic System for Microinjection of Zebrafish Embryos," *PLOS ONE*, vol. 2, no. 9, p. e862, Sep. 2007.

[78] K. Chun, G. Hashiguchi, H. Toshiyoshi, and andHiroyuki Fujita, "Fabrication of Array of Hollow Microcapillaries Used for Injection of Genetic Materials into Animal/Plant Cells," *Japanese Journal of Applied Physics*, vol. 38, no. Part 2, No. 3A, pp. L279–L281, Mar. 1999.

[79] M. Yew, Y. Ren, K. S. Koh, C. Sun, and C. Snape, "A Review of State-of-the-Art Microfluidic Technologies for Environmental Applications: Detection and Remediation," *Global Challenges*, vol. 3, no. 1, p. 1800060, 2019.

[80] Y. Fukui, E. S. Lee, and N. Araki, "Effect of medium renewal during culture in two different culture systems on development to blastocysts from in vitro produced early bovine embryos," *J Anim Sci*, vol. 74, no. 11, pp. 2752–2758, Nov. 1996.

[81] P. Mitchell, "Microfluidics—downsizing large-scale biology," *Nature Biotechnology*, 01-Aug-2001. [Online]. Available: https://www.nature.com/articles/nbt0801_717. [Accessed: 16-Sep-2018].

[82] K.R. Szulwach, P. Chen, X. Wang, J. Wang, L. S. Weaver, M. L. Gonzales, G. Sun, M. A. Unger, "Single-Cell Genetic Analysis Using Automated Microfluidics to Resolve Somatic Mosaicism," *PLOS ONE*, vol. 10, no. 8, p. e0135007, Aug. 2015.

[83] A. G. Vincent, R. W. Pascal, A.D. Beaton, J. Walk, J. E. Hopkins, E. M. S. Woodward, M. Mowlem, M. C. Lohan, "Nitrate drawdown during a shelf sea spring bloom revealed using a novel microfluidic in situ chemical sensor deployed within an autonomous underwater glider," *Marine Chemistry*, vol. 205, pp. 29–36, Sep. 2018.

[84] R. Samuel, H. Feng, A. Jafek, D. Despain, T. Jenkins, and B. Gale, "Microfluidic—based sperm sorting & analysis for treatment of male infertility," *Transl Androl Urol*, vol. 7, no. Suppl 3, pp. S336–S347, Jul. 2018.

[85] J. Song, H. Ryu, M. Chung, Y. Kim, Y. Blum, S. S. Lee, O. Pertz, N. L. Jeon, "Microfluidic platform for single cell analysis under dynamic spatial and temporal stimulation," *Biosensors and Bioelectronics*, vol. 104, pp. 58–64, May 2018.

[86] J. Liu, A. R. Sternberg, S. Ghiasvand, and Y. Berdichevsky, "Epilepsy-on-a-Chip System for Antiepileptic Drug Discovery," *IEEE Transactions on Biomedical Engineering*, vol. 66, no. 5, pp. 1231–1241, May 2019.

[87] W. Liu, J. Song, X. Du, Y. Zhou, Y. Li, R. Li, L. Lyu, Y. He, J. Hao, J. Ben, W. Wang, H. Shi, Q. Wang, "AKR1B10 (Aldo-keto reductase family 1 B10) promotes brain metastasis of lung cancer cells in a multi-organ microfluidic chip model," *Acta Biomaterialia*, vol. 91, pp. 195–208, Jun. 2019.

[88] S. Shin, B. Kim, Y.-J. Kim, and S. Choi, "Integrated microfluidic pneumatic circuit for point-of-care molecular diagnostics," *Biosensors and Bioelectronics*, vol. 133, pp. 169–176, May 2019.

[89] A. Adamo and K. F. Jensen, "Microfluidic based single cell microinjection," *Lab on a Chip*, vol. 8, no. 8, pp. 1258–1261, 2008.

[90] "PDMS: A review," *Elveflow.* .

[91] L. Zhou, G. Zhuang, and G. Li, "A facile method for the fabrication of glass-PDMS-glass sandwich microfluidic devices by sacrificial molding," *Sensors and Actuators B: Chemical*, vol. 261, pp. 364–371, May 2018.

[92] W. Fan, M. Qiao, Y. Jin, H. Zhou, Y. Ge, Q. Jin, J. Zhao, "High efficiency single-cell capture based on microfluidics for single cell analysis," *J. Micromech. Microeng.*, vol. 29, no. 3, p. 035004, Jan. 2019.

[93] E. Kaganovitch, X. Steurer, D. Dogan, C. Probst, W. Wiechert, and D. Kohlheyer, "Microbial single-cell analysis in picoliter-sized batch cultivation chambers," *New Biotechnology*, vol. 47, pp. 50–59, Dec. 2018.

[94] Y. Gao, G. Stybayeva, and A. Revzin, "Fabrication of composite microfluidic devices for local control of oxygen tension in cell cultures," *Lab on a Chip*, vol. 19, no. 2, pp. 306–315, 2019.

[95] Y. Ren, S.-H Huang, S. Mosser, M. O. Heuschkel, A. Bertsch, P. C. Fraering, J.-J. J. Chen, P. Renaud, "A Simple and Reliable PDMS and SU-8 Irreversible Bonding Method and Its Application on a Microfluidic-MEA Device for Neuroscience Research," *Micromachines*, vol. 6, no. 12, pp. 1923–1934, Dec. 2015.

[96] S. McCormick, Z. Tong, A. Ivask, M. Morozesk, N. H. Voelcker, E. Lombi, C. Priest, "Optimization of binding B-lymphocytes in a microfluidic channel: surface modification, stasis time and shear response," *Biofabrication*, vol. 10, no. 1, p. 014101, Nov. 2017.

[97] S.-Y. Tang, R. Qiao, S. Yan, D. Yuan, Q. Zhao, G. Yun, T. P. Davis, W. Li, "Microfluidic Mass Production of Stabilized and Stealthy Liquid Metal Nanoparticles," *Small*, vol. 14, no. 21, p. 1800118, 2018.

[98] A. Shakoor, M. Xie, T. Luo, J. Hou, Y. Shen, J. K. Mills, D. Sun, "Achieve Automated Organelle Biopsy on Small Single Cells Using a Cell Surgery Robotic System," *IEEE Transactions on Biomedical Engineering*, pp. 1–1, 2018.

[99] M. Nakajima, Y. Ayamura, M. Takeuchi, N. Hisamoto, S. Pastuhov, Y. Hasegawa, T. Fukuda, Q. Huang, "High-precision microinjection of microbeads into C. elegans trapped in a suction microchannel," in *2017 IEEE International Conference on Robotics and Automation (ICRA)*, 2017, pp. 3678–3683.

[100] Y.-S. Lee, "3D-printed Microfluidic Control Systems," Thesis, 2018.

[101] W. Takken and T. W. Scott, *Ecological Aspects for Application of Genetically Modified Mosquitoes*. Springer Science & Business Media, 2003.

[102] C. G. Extavour and M. Akam, "Mechanisms of germ cell specification across the metazoans: epigenesis and preformation," *Development*, vol. 130, no. 24, pp. 5869–5884, Dec. 2003.

[103] A. P. Mahowald, "Assembly of the Drosophila germ plasm," in *International Review of Cytology*, vol. 203, Academic Press, 2001, pp. 187–213

[104] N. F. Lobo, J. R. Clayton, M. J. Fraser, F. C. Kafatos, and F. H. Collins, "High efficiency germ-line transformation of mosquitoes," *Nature Protocols*, vol. 1, no. 3, p. 1312, Aug. 2006

[105]   P. J. Kitson, M. H. Rosnes, V. Sans, V. Dragone, and L. Cronin, "Configurable 3D-Printed millifluidic and microfluidic 'lab on a chip' reactionware devices," *Lab on a Chip*, vol. 12, no. 18, pp. 3267–3271, 2012.

[106]   M. P. Lee, G. J. T. Cooper, T. Hinkley, G. M. Gibson, M. J. Padgett, and L. Cronin, "Development of a 3D printer using scanning projection stereolithography," *Scientific Reports*, vol. 5, p. 9875, Apr. 2015.

[107]   Y. Temiz, R. D. Lovchik, G. V. Kaigala, and E. Delamarche, "Lab-on-a-chip devices: How to close and plug the lab?," *Microelectronic Engineering*, vol. 132, pp. 156–175, Jan. 2015.

[108]   R. Amin , S. Knowlton, A. Hart, B. Yenilmez, F. Ghaderinezhad, S. Katebifar, M. Messina, A. Khademhosseini, S. Tasoglu, "3D-printed microfluidic devices," *Biofabrication*, vol. 8, no. 2, p. 022001, Jun. 2016.

[109]   W. Lee, D. Kwon, W. Choi, G. Y. Jung, A. K. Au, A. Folch, S. Jeon, "3D-Printed Microfluidic Device for the Detection of Pathogenic Bacteria Using Size-based Separation in Helical Channel with Trapezoid Cross-Section," *Scientific Reports*, vol. 5, p. 7717, Jan. 2015.

[110]   H. N. Chan, Y. Chen, Y. Shu, Y. Chen, Q. Tian, and H. Wu, "Direct, one-step molding of 3D-printed structures for convenient fabrication of truly 3D PDMS microfluidic chips," *Microfluid Nanofluid*, vol. 19, no. 1, pp. 9–18, Jul. 2015.

[111]   C. I. Rogers, K. Qaderi, A. T. Woolley, and G. P. Nordin, "3D printed microfluidic devices with integrated valves," *Biomicrofluidics*, vol. 9, no. 1, p. 016501, Jan. 2015.

[112]   V. Romanov, R. Samuel, M. Chaharlang, A. R. Jafek, A. Frost, and B. K. Gale, "FDM 3D Printing of High-Pressure, Heat-Resistant, Transparent Microfluidic Devices," *Anal. Chem.*, vol. 90, no. 17, pp. 10450–10456, Sep. 2018.

[113]   M. J. Beauchamp, H. Gong, A. T. Woolley, and G. P. Nordin, "3D Printed Microfluidic Features Using Dose Control in X, Y, and Z Dimensions," *Micromachines*, vol. 9, no. 7, p. 326, Jul. 2018.

[114]   "Understanding Accuracy, Precision, and Tolerance in 3D Printing," *Formlabs*. [Online]. Available: https://formlabs.com/blog/understanding-accuracy-precision-tolerance-in-3d-printing/. [Accessed: 28-Jun-2019].

[115]   B. C. Gross, K. B. Anderson, J. E. Meisel, M. I. McNitt, and D. M. Spence, "Polymer Coatings in 3D-Printed Fluidic Device Channels for Improved Cellular Adherence Prior to Electrical Lysis," *Anal. Chem.*, vol. 87, no. 12, pp. 6335–6341, Jun. 2015.

[116]   M. D. Brennan, M. L. Rexius-Hall, and D. T. Eddington, "A 3D-Printed Oxygen Control Insert for a 24-Well Plate," *PLOS ONE*, vol. 10, no. 9, p. e0137631, Sep. 2015.

[117]   S. Tsuda, H. Jaffery, D. Doran, M. Hezwani, P. J. Robbins, M. Yoshida, L. Cronin, "Customizable 3D Printed 'Plug and Play' Millifluidic Devices for Programmable Fluidics," *PLOS ONE*, vol. 10, no. 11, p. e0141640, Nov. 2015.

[118]   A. S. Jović, M. M. Raković, Đ. S. Čantrak, and N. Z. Janković, "Do-it-yourself microfluidics and possibilities for micro PIV," *FME Transactions*, vol. 46, no. 4, pp. 525–529, 2018.

[119]   Z. Bai, H. Bao, Y. Yuan, X. Yang, Y. Xi, and M. Wang, "Real-time observation of perturbation of a Drosophila embryo's early cleavage cycles with microfluidics," *Analytica Chimica Acta*, vol. 982, pp. 131–137, Aug. 2017.

[120]   Z. Strike, K. Ghofrani, and C. Backhouse, "CO2 Laser-Based Rapid Prototyping of Micropumps," *Micromachines*, vol. 9, no. 5, p. 215, May 2018.

[121]   J. Kim, R. Surapaneni, and B. K. Gale, "Rapid prototyping of microfluidic systems using a PDMS/ polymer tape composite," *Lab on a Chip*, vol. 9, no. 9, pp. 1290–1293, 2009.

[122]   Y. Ma, W. Chang, C. Wang, S. Liu, W. Yen, K. Luo, H. You, J. Wu, M. S. Lee, G. Lee, "A self-driven microfluidic chip through a rapid surface modification of PDMS and its application for digital loop-mediated amplification (LAMP)," in *2016 IEEE 11th Annual International Conference on Nano/Micro Engineered and Molecular Systems (NEMS)*, 2016, pp. 1–4.

[123]   S. Kim, D. Dehlinger, J. Peña, H. Seol, M. Shusteff, N. M. Collette, M. Elsheikh, M. Davenport, P. Naraghi-Arani, E. Wheeler, "Virus concentration and purification by a microfluidic filtering system with an integrated PEGylated antifouling membrane," *Microfluid Nanofluid*, vol. 23, no. 1, p. 9, Jan. 2019.

[124]   S. Satyanarayana, R. N. Karnik, and A. Majumdar, "Stamp-and-stick room-temperature bonding technique for microdevices," *Journal of Microelectromechanical Systems*, vol. 14, no. 2, pp. 392–399, Apr. 2005.

[125]   A. Yilmaz and M. Utz, "Characterisation of oxygen permeation into a microfluidic device for cell culture by in situ NMR spectroscopy," *Lab on a Chip*, vol. 16, no. 11, pp. 2079–2085, 2016.

[126]   B. Pečar, M. Možek, and D. Vrtačnik, "Thermoplastic - PDMS Polymer Covalent Bonding for Microfluidic Applications," *Informacije MIDEM*, vol. 47, no. 3, pp. 147–154, Dec. 2017.

[127]   M.-E. Vlachopoulou, A. Tserepi, P. Pavli, P. Argitis, M. Sanopoulou, and K. Misiakos, "A low temperature surface modification assisted method for bonding plastic substrates," *J. Micromech. Microeng.*, vol. 19, no. 1, p. 015007, Nov. 2008.

[128]   J. K. Lee, K.-W. Park, J. C. Choi, H.-R. Kim, and S. H. Kong, "Design and fabrication of PMMA-micromachined fluid lens based on electromagnetic actuation on PMMA–PDMS bonded membrane," *J. Micromech. Microeng.*, vol. 22, no. 11, p. 115028, Oct. 2012.

[129]   Saffman Philip Geoffrey and Taylor Geoffrey Ingram, "The penetration of a fluid into a porous medium or Hele-Shaw cell containing a more viscous liquid," *Proceedings of the Royal Society of London. Series A. Mathematical and Physical Sciences*, vol. 245, no. 1242, pp. 312–329, Jun. 1958.

[130]   A. D. McEwan and G. I. Taylor, "The peeling of a flexible strip attached by a viscous adhesive," *Journal of Fluid Mechanics*, vol. 26, no. 1, pp. 1–15, Sep. 1966.

[131]   S. Bhattacharya, A. Datta, J. M. Berg, and S. Gangopadhyay, "Studies on surface wettability of poly(dimethyl) siloxane (PDMS) and glass under oxygen-plasma treatment and correlation with bond strength," *Journal of Microelectromechanical Systems*, vol. 14, no. 3, pp. 590–597, Jun. 2005.

[132]   "Green Fluorescent Protein (GFP) - US." [Online]. Available: https://www.thermofisher.com/us/en/home/life-science/cell-analysis/fluorophores/green-fluorescent-protein.html. [Accessed: 21-Sep-2018].

[133]   Y. T. Chow, S. Chen, C. Liu, C. Liu, L. Li, C. W. M. Kong, S. H. Cheng, R. A. Li, D. Sun, "A High-Throughput Automated Microinjection System for Human Cells With Small Size," *IEEE/ASME Transactions on Mechatronics*, vol. 21, no. 2, pp. 838–850, Apr. 2016.
.